ACS OMEGA

Open Access

http://pubs.acs.org/journal/acsodf

Article

Machine Learning Assisted Prediction of Porosity and Related Properties Using Digital Rock Images

Md Irfan Khan and Aaditya Khanal*

Cite This: *ACS Omega* 2024, 9, 30205−30223

Read Online

ACCESS | Metrics & More | Article Recommendations

ABSTRACT: Accurately estimating reservoir rock properties is paramount for modeling the storage and flow of fluids (hydrocarbon, carbon dioxide, and groundwater) in porous media. However, existing laboratory techniques to measure rock properties are usually time-consuming, expensive, and computationally intensive. This work proposes an efficient workflow that uses the machine learning algorithm, based on the convolutional neural network (CNN) framework, to predict rock properties from microcomputed tomography (micro-CT) X-ray images. The workflow involves data preprocessing, label extraction, training, and prediction using the segmented images of the rock to predict porosity, throat area, and pore surface area, which are essential for pore-scale modeling. The model was trained and validated on the Bentheimer sandstone, which was then used to predict properties of other sandstones (Castlegate and Leopard) with different pore structures and flow properties. The model yielded a good prediction for the throat and pore surface area but a significant error for porosity. Subsequently, a new complex model was trained and validated using diverse images from Bentheimer and an additional rock Castlegate, which was then used to predict the properties of Leopard sandstone. The new model improved the prediction of each property, resulting in mean absolute percentage error (MAPE) values of 2.19%, 3.04%, and 6.08% for porosity, pore surface area, and throat area with the binary images, respectively. In addition, we present a novel data-driven method using a simple regression model to predict the absolute permeability of a digital rock sample using the pore network parameters as predictors. The extreme gradient boost (XGBoost), which performed the best among several machine algorithms, was trained and validated using digital rock images from Bentheimer and Castlegate sandstone. The generated model was then used to predict the absolute permeability of the Leopard sandstone with an R^2 of 0.813, which was a significant improvement over the model generated solely by using either the Bentheimer or the Castlegate sandstone images. Furthermore, our analysis showed that the tortuosity had the most significant effect on the absolute permeability prediction of the rock sample. This study showed that we can reliably predict the morphological properties of porous media using computationally efficient models generated from digital rock images, which can be used to build a regression model to predict the crucial petrophysical properties needed to model the flow of fluids in porous media.

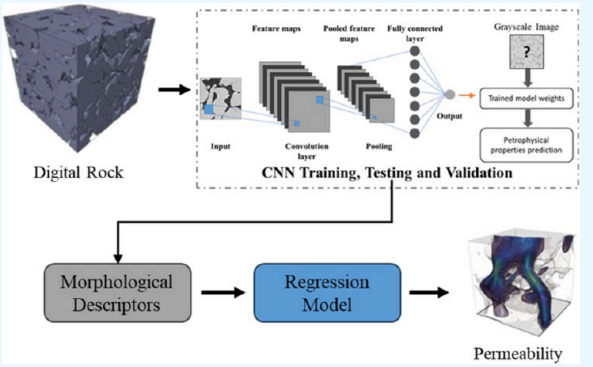

1. INTRODUCTION

The reservoir rocks contain complex networks of interconnected and isolated pores, which create an ideal environment for trapping hydrocarbons in the porous media. Furthermore, the connected pore networks dictate the flow behavior and production potential of the trapped hydrocarbons by directly affecting the intrinsic permeability.[1] Thus, the accurate determination of the reservoir rock properties, such as porosity, throat area, and permeability, is essential for predicting the initial hydrocarbon in place, estimating the ultimate recovery, identifying the storage potential for CO_2 sequestration and hydrogen storage, and modeling groundwater flow in subsurface porous media.[2−4] These properties are usually determined from reservoir rock samples or the core through routine and special core analyses (RCA/SCAL) in the lab. The fundamental properties, such as porosity, are measured during the RCA, whereas other complex properties (capillary pressure, relative permeability, and wettability) require SCAL. However, the data collected from the core analysis may have significant errors due to issues such as the presence of hydratable clays, miscalibration of equipment, absorption of atmospheric water in the core, loss of core samples due to chipping, and other reasons.[5] As a result, the core analysis data may not always be reliable for modeling the storage and flow behavior of the reservoir rocks.[6] For these

Received: December 22, 2023
Revised: April 9, 2024
Accepted: May 7, 2024
Published: June 25, 2024

reasons, there is a significant push toward reliable and economical alternative and complementary methods to estimate these properties. The three-dimensional rock images obtained from advanced imaging techniques, often referred to as the "digital rock", provide an alternative to laboratory-based methods.

Digital rock technology is an effective and accepted tool for extracting various petrophysical and flow properties from reservoir rocks. Numerical simulation can be applied to data obtained from digital rocks to compute mechanical properties,[7,8] predict fluid topology,[9] estimate flow properties,[10,11] and identify electrical properties[12] of the rock by solving the governing equations of different pore-scale phenomena. The typical digital rock physics workflow can be divided into the following steps: (a) acquiring raw grayscale digital rock images, (b) segmentation of digital rock images, and (c) calculating petrophysical properties by numerical simulation.[13] Segmentation is a process of identifying all the phases (pore vs matrix) in an image correctly and distinctly. This process is crucial in digital rock analysis and influences pore-scale characterization.[14,15] Inaccurate segmentation of the digital rock leads to significant errors in subsequent quantitative analysis. There are numerous segmentation methods, among which machine learning (ML) algorithms are becoming more popular due to their relative accuracy and ease over traditional methods.[16,17] ML methods have been found to be useful in solving complex problems in several areas of science and engineering by identifying relationships between inputs and outputs, deciphering patterns, and generating solutions to complex problems. Petroleum industry also finds extensive use of ML in different areas, including reservoir engineering,[18] production engineering,[19] drilling engineering,[20] and other related areas.[21,22]

The application of ML continues to grow for other engineering domains, including digital rock analysis for property and flow behavior estimation. Tembely and AlSumaiti[23] developed a workflow for fast and accurate prediction of the permeability of complex networks using deep learning methods. Their work suggested that the deep neural network performs slightly better than gradient boosting and linear regression for the permeability calculation. Linden et al.[24] investigated the relationship between fluid flow at the macroscale and internal pore structure in porous media by applying machine learning techniques. They reported that the pore network closeness centrality, a metric for describing the centrality of the shortest paths between pores, was the most crucial network feature to predict the permeability. Many researchers incorporate physical equations into ML to reduce the dependency on the data. This method is usually referred to as physics-informed machine learning.[25] Tian et al.[26] suggested a combination of artificial neural networks (ANNs) and genetic algorithms to predict permeability. Their study uses the genetic algorithm to tune the ANN architecture, whereas the ANN is applied to learn the nonlinear relationships. They reported that tortuosity, number of pores, and pore−throat ratio were inversely proportional to permeability. There are other studies that focus on the prediction of flow properties,[27,28] but studies for the prediction of pore networks and porosity remain limited.

The convolutional neural network (CNN) is capable of extracting task-related data from the images with high accuracy; hence, in many studies,[29,30] a CNN-based surrogated model has been conducted to predict rock permeability. However, the use of CNN is not out of the scope of limitations. First, a CNN model requires a large number of training data for better prediction, and acquiring high-quality 3D images of rock samples is expensive. This complexity may explain why, in many previous studies,[31−33] artificially generated sphere packs are used to predict the petrophysical properties of rock samples. Second, the 3D CNN algorithm is highly computationally intensive and requires excessive memory.[34] In contrast, simple regression models like random forest (RF), support vector machine (SVM), and gradient boost (GB) algorithms are much easier to interpret and less memory intensive.[35,36] Further investigation is required to define a systematic workflow focusing on data preprocessing and predicting various petrophysical properties and microstructural characteristics of a digital rock sample. Furthermore, although numerous previously published works have used an image-based approach using CNN to predict permeability, significantly less focus has been placed on simple regression models, which are computationally less intensive than CNN.

In this work, a step-by-step procedure for predicting the morphological descriptors, namely, porosity (Ø), pore surface area (PSA), and throat area (TA) from the digital rock, is presented using a convolutional neural network (CNN). Utilizing the framework, the end user can extract the properties related to the pore network of an unknown rock sample using only raw micro-CT images, which can later be used to build a data-driven machine-learning model to predict permeability. To train the machine-learning model using CNN, we used micro-CT images of multiple rocks (Bentheimer, Castlegate, and Leopard sandstones) with different pore structures. The trained model is then used to predict the morphological properties of other rocks with different properties. First, three models are trained with binary and grayscale images of two different rocks. Two of these models are only trained with images of either Bentheimer and Castlegate sandstone. The third model is trained with the images of both Bentheimer and Castlegate sandstone. Next, the trained model was used to predict the properties of Leopard sandstone, which were unseen by each of the three models. Our investigation reveals that predata processing of the rock images significantly improves prediction accuracy; thus, this is a crucial step. In addition, the results showed that skewed data sets and defective images could negatively affect the performance of the trained model. The novel workflow presented here expands on the limited literature for porosity and related property prediction using ML methods. We utilized actual rock images instead of synthetic images. While synthetic images have advantages,[37−39] we believe that actual rock images provide a more realistic representation of porous media structure and properties. We focused on the quantitative analysis of rock images, specifically measuring pore-related properties and their distribution. While previous studies have primarily used imaging techniques such as thin section, CT scan, and SEM images to qualitatively analyze rocks,[40−42] our approach provides a more comprehensive and quantitative understanding of the rock properties. We further developed a data-driven machine learning model to predict the absolute permeability of a new rock sample by using the properties extracted from the pore network of known rock samples. This study confirms that a simple regression model can be developed to predict permeability by using accurate morphological descriptors of porous media. In addition, our study offers practical techniques for image preprocessing and segmentation, which can be useful for other geoscientists working with similar types of data. The remainder of the paper is organized as follows: Section 2 provides a brief description of the materials (rock

https://doi.org/10.1021/acsomega.3c10131
ACS Omega 2024, 9, 30205−30223

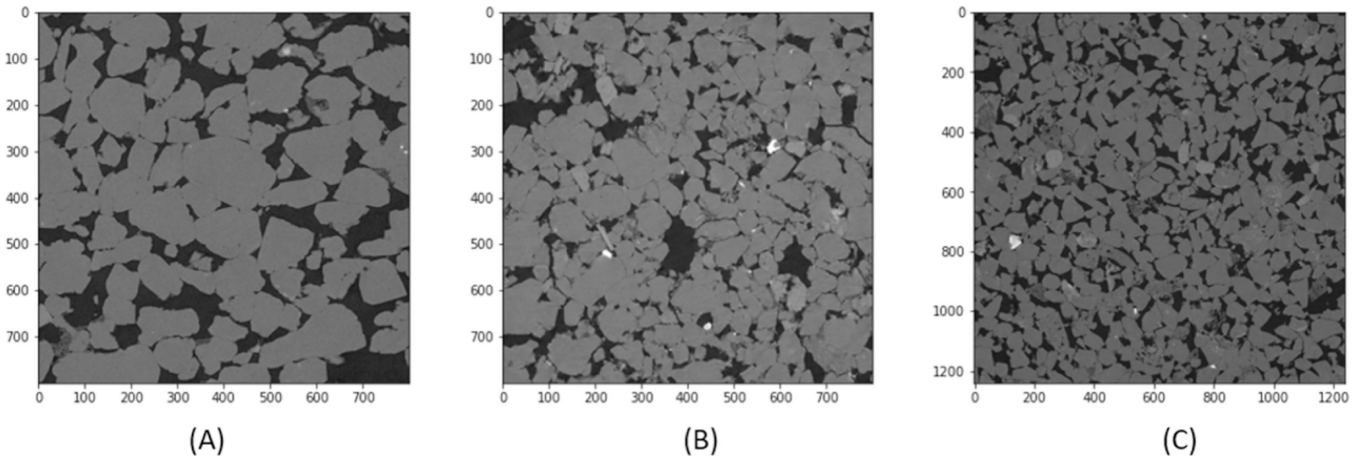

Figure 1. Tomogram layer of (A) Bentheimer sandstone, (B) Castlegate sandstone, and (C) Leopard sandstone.

samples) used in this study, and Section 3 presents the methods for image segmentation, label extraction, and machine learning model architectures. Section 4 is dedicated to the results and discussion of this study. Finally, Section 5 provides a summary and significant conclusions from this work.

2. MATERIALS

This study uses three digital rock samples: Bentheimer, Castlegate, and Leopard. The Bentheimer sandstone is selected as it is considered to be the model sandstone for reservoir studies,[43] and the other two rocks (Castlegate and Leopard) are chosen as they have similar fractions of the primary minerals as Bentheimer sandstone: quartz, feldspar, and kaolinite. The digital versions of these sandstones contain micro-CT images in the netCDF format and are collected from the "Digital Rock Portal".[44] The Bentheimer sandstone has a lab-measured average porosity of 23.5% and a permeability of 1.30 Darcy.[43,45] The porosity of the Castlegate and Leopard sandstone is 26.0% and 22.8%, respectively, and the corresponding permeability is 1.05 and 0.08 Darcy, respectively.[45] Further details on the other properties of the selected rock samples are given in Shikhov et al.[45] Figure 1 displays the Bentheimer, Leopard, and Castlegate sandstone subsamples, and Table 1 provides the specifics of the tomograms.

Table 1. Size and Resolution of the Tomograms of Bentheimer, Castlegate, And Leopard Sandstone

Sandstone name	Size (voxels)	Resolution (μm)
Bentheimer	800 × 800 × 400	2.15
Leopard	1240 × 1240 × 180	2.15
Castlegate	800 × 800 × 400	2.28

3. METHODS

This section discusses the methods used to prepare the raw grayscale images and extract the morphological properties (Ø, TA, and PSA) and the absolute permeability. In addition, the machine learning models with different training and testing functions for predicting the morphological properties and permeability are also briefly described. Figure 2 shows the general workflow for predicting the morphological properties from the digital rock image, which involves image acquisition from digital rock, preprocessing of raw grayscale images (augmentation, data cleaning, denoising), segmentation of the images, extracting the labels from binary and grayscale images, preprocessing of the label data, creating a CNN model, and finally testing, training, and validation of the CNN model.

Figure 3 shows the workflow for developing a regression model to predict the permeability. The workflow involves subdividing the rock samples, segmenting the images, extracting input and target parameters, and finally training, testing, and evaluating the accuracy of the regression model. Additional details on each step and the relevant morphological properties are provided in Section 3.2.2.

3.1. Image Acquisition and Pre-processing of Data.

Data pre-processing is a crucial machine learning step as it significantly affects model accuracy. As a part of data pre-processing, we applied data cleaning, denoising, and augmentation to the input data set and data transformation to the target data set. Data cleaning is a process of detecting incorrect and noisy data and correcting or removing it from the data set. Usually, the micro-CT images have noise and some artifacts,[46] which can lead to incorrect label extraction. After extracting the 2D images, the 3D tomographic data, and subdividing them into the regions of interest (ROIs) measuring 200 × 200 pixels, it was observed that some images have higher noise labels (Figure 4). Hence, we manually checked the input images before any further steps and deleted the images which had higher noise interference. We applied a Gaussian blur filter to reduce the signal-to-noise ratio of the rest of the images, as the Gaussian blur filter effectively smooths out noise while preserving crucial features of the image.[47]

As the voxel sizes of the individual rock samples are different (Table 1), dividing the 3D tomograms into specific ROIs yields a variable number of images. For instance, the Bentheimer sandstone sample has 6400 ROI with 16 images per 400 layers. In order to improve the predictive ability of the trained model, we increased the number of training data by augmentation. The data augmentation is implemented in this work by rotating the images at different angles (90°, 180°, and 270°). After cleaning the data set and data augmentation, 24,880 images were generated, from which 17,416 images were used to train the model, 3,732 images for testing, and 3,732 for validation. The label data was then checked for skewness factor, as it can significantly impact the model's ability to predict outcomes accurately. A skewed data set has a significant deviation between the value of the mean and median. So, the tail region of the skewed data set may act as an outlier, and outliers negatively affect the model's performance.[48] In this work, the values of the

https://doi.org/10.1021/acsomega.3c10131
ACS Omega 2024, 9, 30205−30223

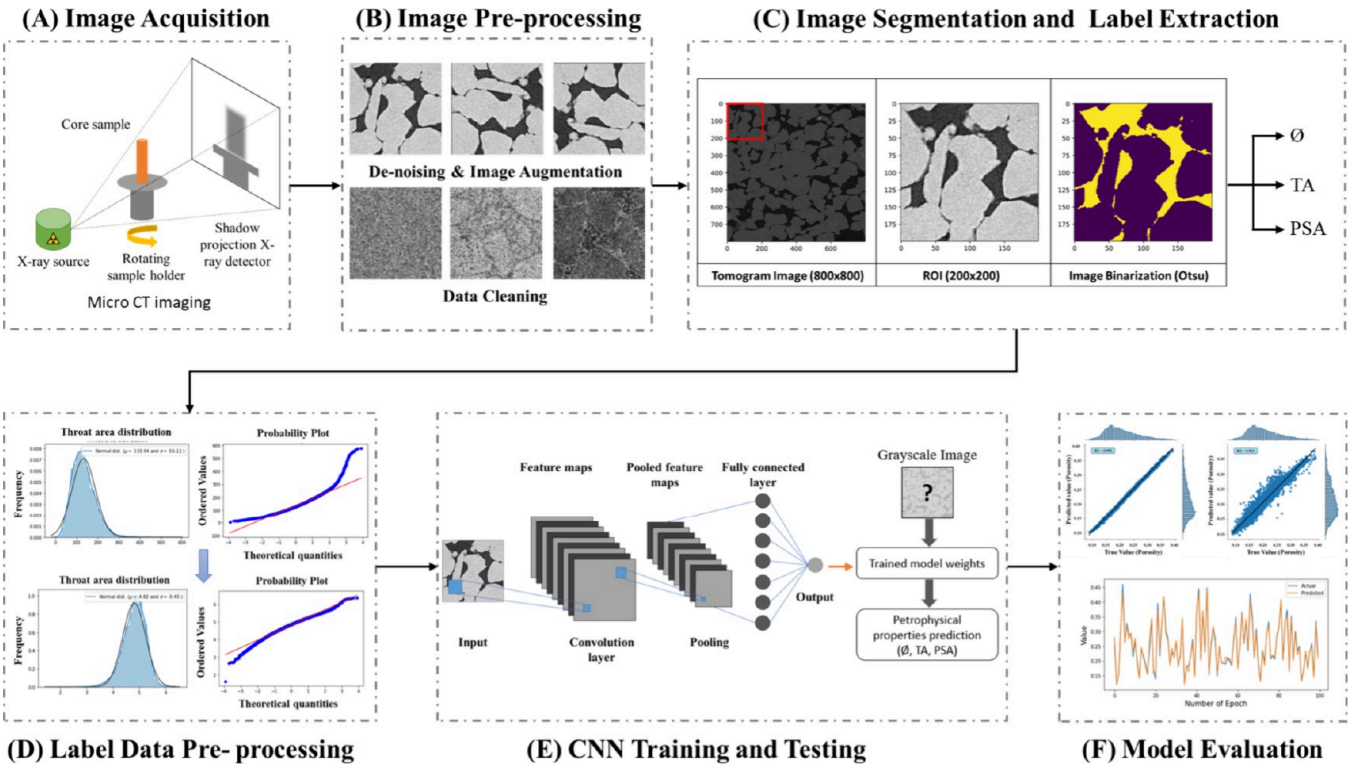

Figure 2. Workflow for extracting and predicting physical properties of porous media using CNN: (A) Image acquisition, (B) Raw image pre-processing (augmentation, data cleaning, denoising), (C) Image segmentation and label data extraction, (D) Label data pre-processing, (E) Training and testing of the CNN model, and (F) and Model evaluation.

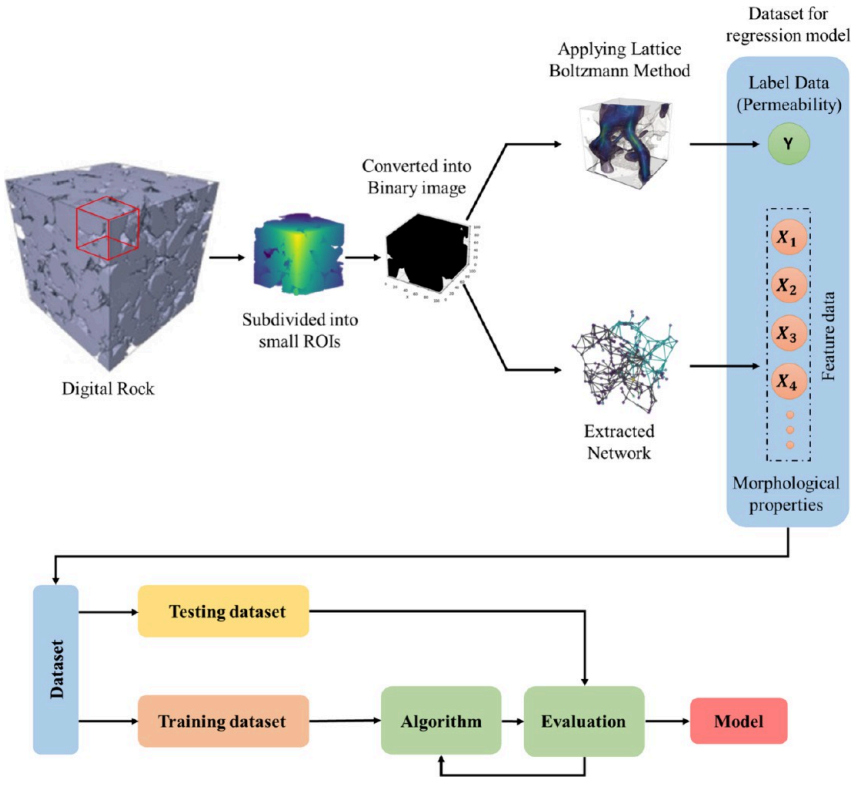

Figure 3. Workflow for developing the regression model to predict permeability.

throat area were positively skewed, and log transformation was applied to the target data set to create normally distributed training data.

3.2. Image Segmentation and Target Data Extraction.

3.2.1. Image Segmentation. The ground truth or the labels for training the ML model were obtained from the binary images

https://doi.org/10.1021/acsomega.3c10131
ACS Omega 2024, 9, 30205−30223

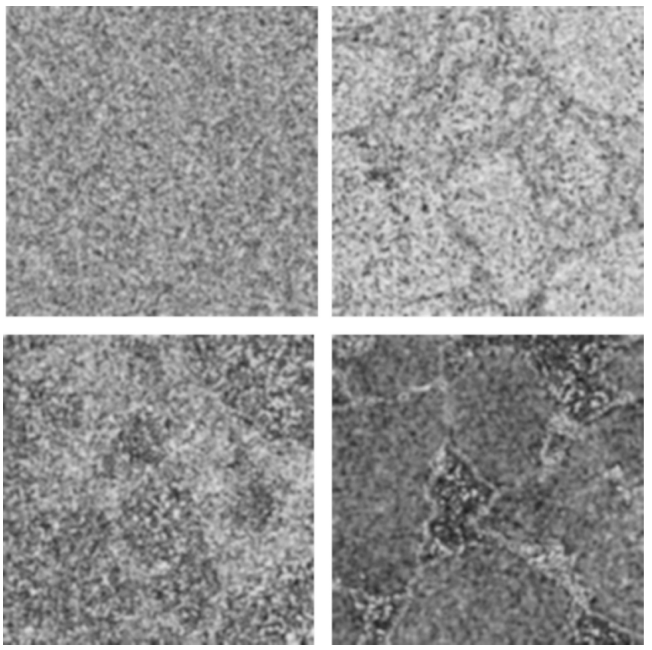

Figure 4. Defective ROIs of Leopard sandstone.

and extracted pore network, which require image segmentation. First, we manually segmented 50 images of each rock sample to create the ground truth using the interactive learning and segmentation toolkit, Ilastik.[49] After that, the segmented results from the traditional thresholding method and a machine learning model were compared with the manually segmented images to evaluate each segmentation method.

The Otsu thresholding[50] method was used as a traditional thresholding tool to segment the individual rock ROIs. The Otsu threshold separates the pixels into the foreground and background. It involves iterating through all possible threshold values and calculating the spread of the foreground and background pixels.[50] The algorithm aims to identify the threshold value at which the sum of foreground and background pixels is the least. "Scikit-image",[51] an image-processing library in Python, was used to implement the Otsu threshold to raw grayscale images to create binary images.

A U-Net model was developed as a machine learning model to segment the individual ROIs of the rock samples. The model architecture is illustrated in Figure 5. Due to the encoder–decoder architecture, the U-Net model can capture both high-level features and fine details of the image. The skip connection option facilitates U-Net to preserve the spatial information of the image. In total, 14,000, 500, and 50 images were used for training, validating, and testing the model, respectively.

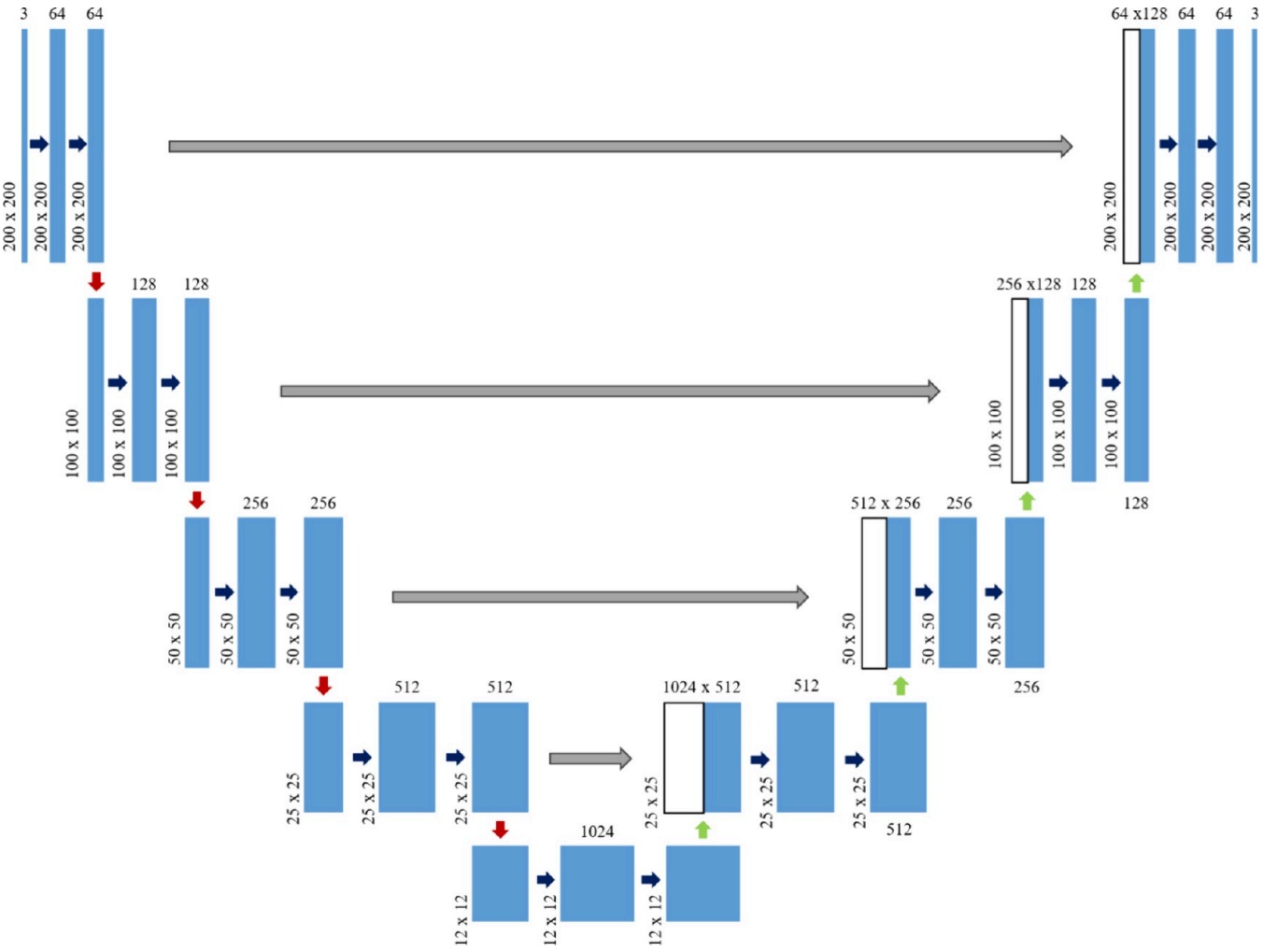

Figure 5. U-Net model architecture for image segmentation.

https://doi.org/10.1021/acsomega.3c10131
ACS Omega 2024, 9, 30205−30223

The intersection over union (IoU) was calculated by comparing the segmented images from the Otsu thresholding method and U-Net model with the manually segmented images (Table 2). The results show that both Otsu and U-Net's

Table 2. Image Segmentation Results from the U-Net Model and the Otsu Thresholding Method

Sandstone type	IoU value for U-Net	IoU value for Otsu thresholding
Bentheimer	0.970	0.954
Leopard	0.805	0.780
Castlegate	0.964	0.949

performance is satisfactory in segmenting the digital rock images. Though U-Net's deep learning approach offers more versatility and capability for complex image segmentation challenges, this study used the Otsu thresholding method to segment the individual ROIs of different rock samples because of simplicity, fast processing, and interpretability. However, it should be noted that for complex images, ML methods trained on a large number of images perform better than traditional thresholding methods.

3.2.2. Morphological Property Extraction. To measure the porosity, first, the pixels of the binary images were separated according to their intensity. For example, the white pixels have an intensity closer to 255 and represent the pore area. Then, the total number of pore pixels was added up, and finally, the porosity was calculated by dividing it by the area of the image. The average porosity calculated from this workflow matches the porosity obtained from the laboratory measurements reported in the literature.[43]

The pore network was extracted from the segmented images using the method proposed by Gostick.[52] This technique uses the watershed algorithm to create a distance map of the segmented image to locate the pores and throats in the tomograms. After the peaks from the watershed were identified using the maximum filter, the spurious peaks on saddles and plateaus of the distance map are eliminated. Following that, the algorithm automatically merges the nearby peaks and considers them as a single large pore. Finally, in order to achieve the segmented pore areas and extracted pore networks, a marker-based watershed algorithm was used. The value of sigma in the Gaussian filter was set to 0.4, and the radius of the spherical structuring element was set to 4, which is similar to the settings suggested by Gostick.[52] Figure 6 summarizes the steps for data processing involved in pore network extraction.

Next, the morphological descriptors for predicting the permeability were extracted from the pore network model. The pore network model represents the network topology of the porous media in terms of their interconnected pores and throats. Table 3 lists the morphological descriptors extracted from the rock sample to create a data-driven model to predict absolute permeability.

Table 3. Morphological Properties Extracted for the Quantitative Characterization of Porous Microstructures

Index	Morphological descriptors	Denotation
1	Porosity	Ø
2	Pore volume	v_p
3	Pore surface area	S_p
4	Maximum pore size	d_{mp}
5	Pore region volume	v_{pr}
6	Pore size distribution	p_d
7	Pore diameter	d_p
8	Maximum throat size	d_{mt}
9	Pore equivalent diameter	d_{eqp}
10	Throat diameter	d_t
11	Throat length	l_t
12	Throat volume	v_t
13	Throat size distribution	t_d
14	Pore inscribed diameter	d_{ip}
15	Pore extended diameter	d_{ep}
16	Throat inscribed diameter	d_{it}
17	Throat total length	l_{Tt}
18	Throat perimeter	l_t
19	Throat cross-sectional area	S_{ct}
20	Throat equivalent diameter	d_{eqt}
21	Throat spacing	m_t
22	Effective diffusivity	D_{eff}
23	Tortuosity	τ

3.2.3. Permeability Extraction. The 3D tomogram of the sandstone was first subdivided into small ROI (100 × 100 × 100) to ease the computational resource requirements prior to permeability calculation. An increment of 100 was applied in each direction to increase the data set. Then, the images were segmented using the Otsu thresholding to distinguish and label

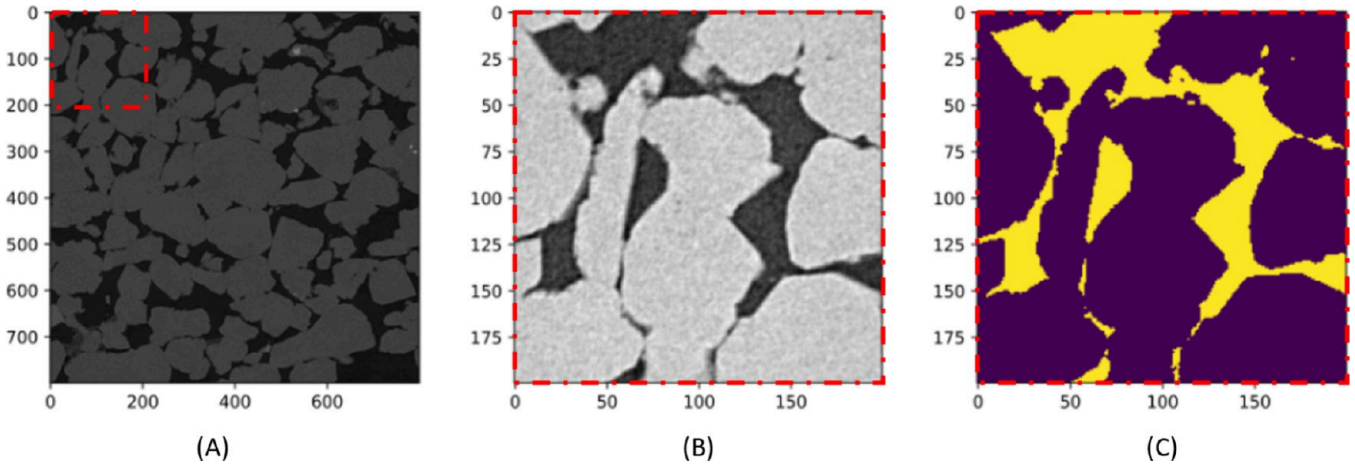

Figure 6. (A) Tomogram of a raw grayscale image for Bentheimer sandstone, (B) ROI (200 × 200) of the tomogram, and (C) segmented image.

https://doi.org/10.1021/acsomega.3c10131
ACS Omega 2024, 9, 30205−30223

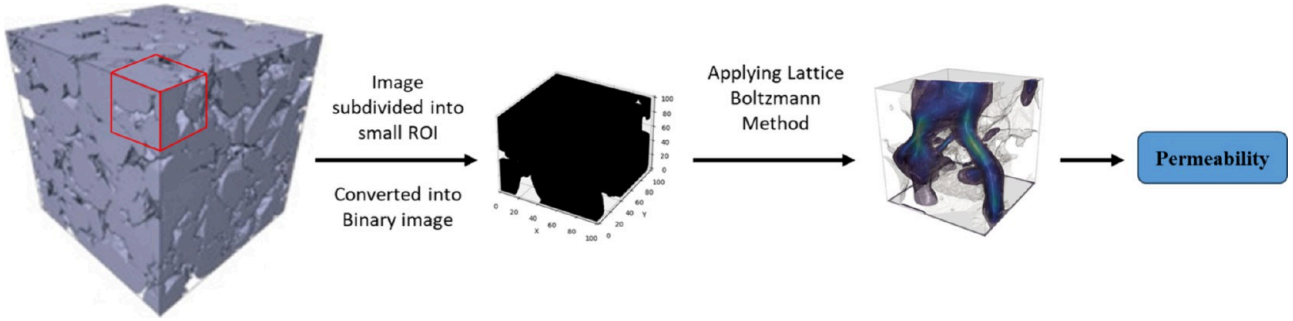

Figure 7. Workflow for extracting permeability from a digital rock image.

solid grains and pore space. After that, based on the defined geometry and grid resolution, a computational mesh was generated using Palabos, and absolute permeability for each block was measured. Palabos,[53] an open-source software library, was used to implement the Lattice Boltzmann Method (LBM) for simulating fluid flow. LBM is a popular numerical method for simulating fluid dynamics in porous media. It is a numerical approach that simulates fluid flow in porous media by representing the fluid as a collection of particles. Each particle is associated with a particle velocity distribution function located at each discrete lattice node. At regular time intervals, the particles collide with one another, and the properties associated with the lattice nodes are updated accordingly. These collisions are governed by rules designed to ensure that the time-averaged motion of the particles aligns with the Navier−Stokes equations,[54] which describe the motion of fluids in a continuum. We used the D3Q19 scheme, representing three-dimensional fluid motion and utilizing 19 associated velocity vectors. Palabos calculates the permeability of the porous medium using Darcy's law.[55] The workflow for extracting the permeability is illustrated in Figure 7.

3.3. Machine Learning Models. *3.3.1. Convolutional Neural Network for the Morphological Property Prediction.* The convolutional neural network (CNN) architecture uses multiple layers of nonlinear transformations, which are trained iteratively to make predictions close to the expected ground truth targets. The CNN consists of convolution, pooling, and fully connected layers (Figure 8).

The function of the first two layers (convolution and pooling) is to extract the features, and the function of the third layer (fully connected layer) is to map the extracted features into the final output. The convolution layers preserve the spatial relationship between inputs and feature maps, whereas fully connected layers do not preserve the spatial structure of their inputs. In CNN, detectors trained by the filters can be reused several times throughout the input image, which makes CNN suited for computer vision tasks. In this study, the inputs for the CNN model were the ROIs obtained from the 2D images, which were generated from the 3D tomographic data. Figure 9 shows the model architecture proposed in this work. In the following sections, we briefly discuss the rationale for choosing the major functions used in this study (ReLU, Dropout, Max-pooling, Adam optimizer, and Huber loss) and their working principle.

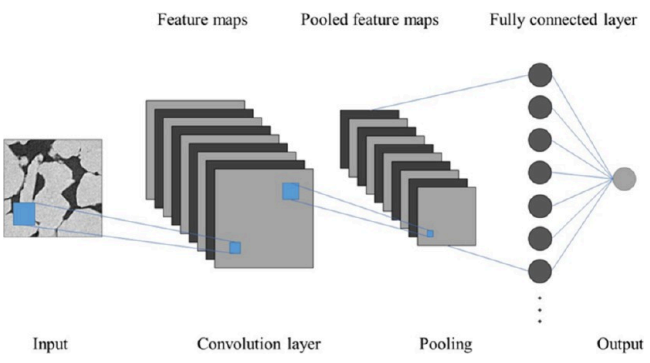

Figure 8. Structure of the convolutional neural network.

The convolutional layer convolves over the input image using filters to extract the key features such as pore and throat spaces, which are important for analyzing the porosity, pore surface area, and throat area of the sandstone. Figure 10 shows the sequential feature extraction at each activation layer from a single ROI using the proposed CNN model.

The convolution process is just a simple mathematical operation of two matrices. For example, consider that an input image has a matrix of (7×7); the filter has a matrix of (3×3); the stride is 2; and the padding is the same. Then, a sum-product operation between the individual elements of the two matrices was done to generate the elements of the feature map with a matrix of (3×3). Equation 1 controls the output dimension of the convolutional process.

$$\left|\frac{n + 2p - f}{S} + 1\right| \times \left|\frac{n + 2p - f}{S} + 1\right| \quad (1)$$

where $n \times n$ is the dimension of the matrix; p is the padding; f is the filter size; and S is the stride.

The activation function introduces nonlinearity into the output of a neural network, allowing it to model more complex relationships between inputs and outputs. There are several activation functions to construct the CNN, such as Sigmoid, Tanh, Softplus, and the Rectified Linear Unit (ReLU). In this work, ReLU was used as an activation function as it is simple to calculate, has a higher convergence speed, is cost-effective, and prevents the emergence of vanishing gradient problems, which is common for Sigmoid and Tanh functions.[56]

Pooling and subsampling were used to reduce the spatial size, hence reducing the number of features and computational complexity of the network. Three standard functions can be used in the pooling operation: average pooling, maximum pooling, and minimum pooling. The max-pooling function with a kernel size of (2×2) and stride of 2 pixels was applied for the images used in this work. The purpose of the max-pooling function is to downsample the input representation by picking up the highest value from the region of the feature map covered by the filter, which tends to retain the most prominent features and edges present in the image. In contrast, average pooling and min pooling can potentially blur important image details and may

https://doi.org/10.1021/acsomega.3c10131
ACS Omega 2024, 9, 30205−30223

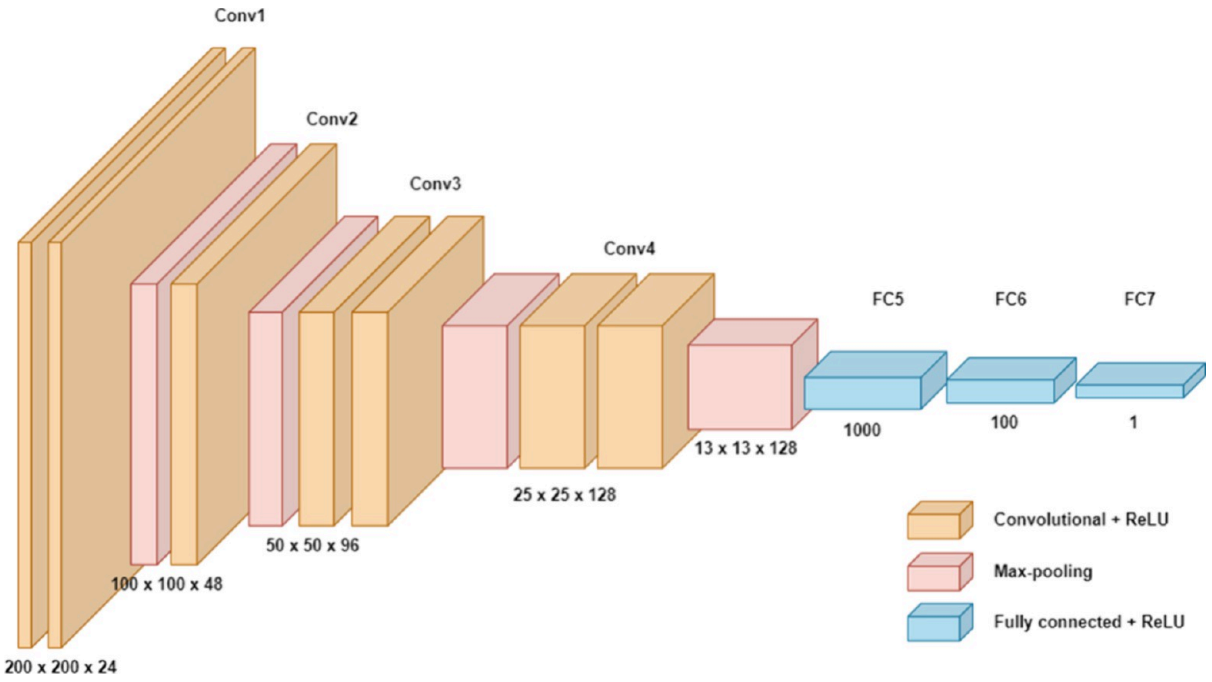

Figure 9. Proposed CNN model architecture.

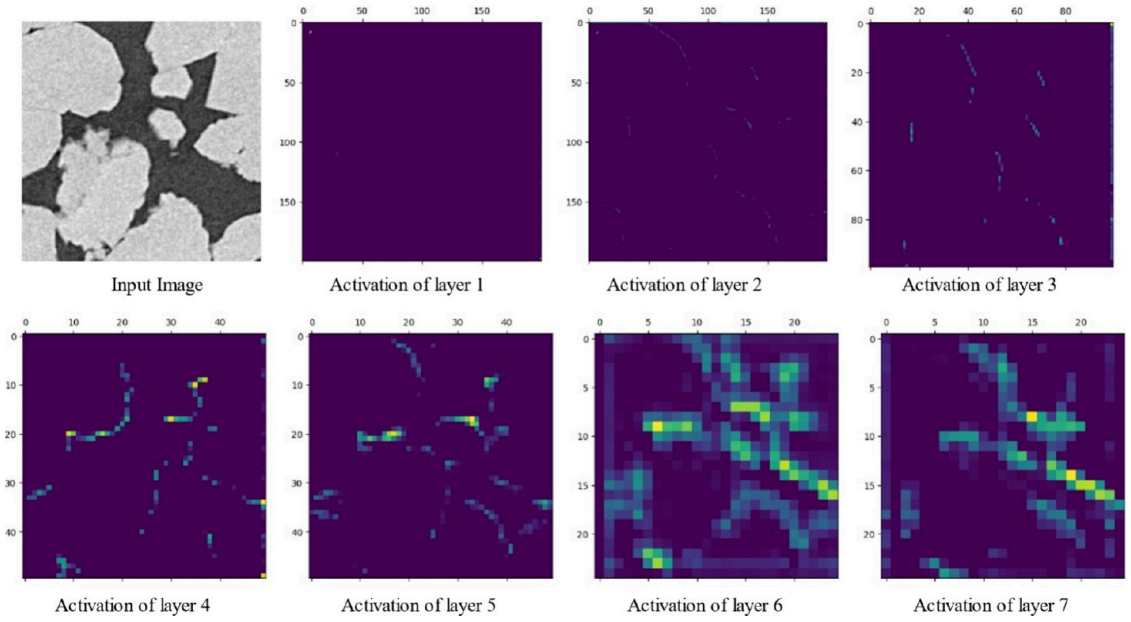

Figure 10. Key feature extraction using the proposed CNN model.

not be as effective at capturing the essential characteristics of the image. Figure 11 illustrates the maximum-pooling operation in CNNs.

The "dropout" method was applied to the fully connected layer to avoid overfitting the training data. After implementing dropout, the network becomes thinner than the standard neural network, thus enhancing the resistance of overfitting and making training faster.[57] In this work, 20% of the neurons in the fully connected layers were dropped out.

The model was trained to minimize errors between its predictions and expected ground truth labels. In this work, "Huber loss"[58] was used as a loss function to compute the error (eq 2). Huber loss is the hybrid of Mean Absolute Error (MAE) and Mean Squared Error (MSE) loss functions, and it takes the

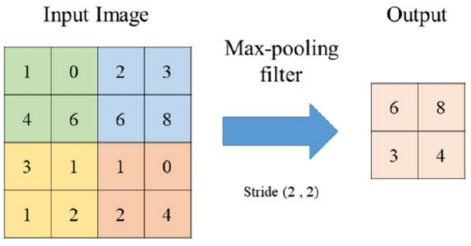

Figure 11. Max-pooling operation in CNNs.

best of these loss functions: robustness and stability. Equation 2 was used to measure the distance and backpropagate the error through the network to compute gradients. The hyperparameter

https://doi.org/10.1021/acsomega.3c10131
ACS Omega 2024, 9, 30205−30223

Table 4. Comparison between Different Evaluation Functions for Model A, Model B, and Model C

Evaluation functions	Porosity		Pore surface area		Throat area	
	Binary image	Grayscale image	Binary image	Grayscale image	Binary image	Grayscale image
Model A (Trained with Bentheimer Images)						
MAPE (%)	1.01	1.43	3.2	4.21	1.97	2.55
MSPE (%)	0.02	0.04	0.18	0.29	0.07	0.11
RMSPE (%)	1.24	1.95	4.29	5.37	2.7	3.34
Model B (Trained with Castlegate Images)						
MAPE (%)	0.84	1.51	3.44	3.93	7.31	2.91
MSPE (%)	0.0136	0.201	0.1589	0.3187	0.867	0.139
RMSPE (%)	1.169	4.49	3.986	5.645	9.311	3.73
Model C (Trained with Bentheimer and Castlegate Images)						
MAPE (%)	3.9	4.13	2.26	3.29	1.17	1.28
MSPE (%)	0.25	0.28	0.08	0.19	0.02	0.03
RMSPE (%)	5.03	5.31	2.93	4.41	1.4	1.66

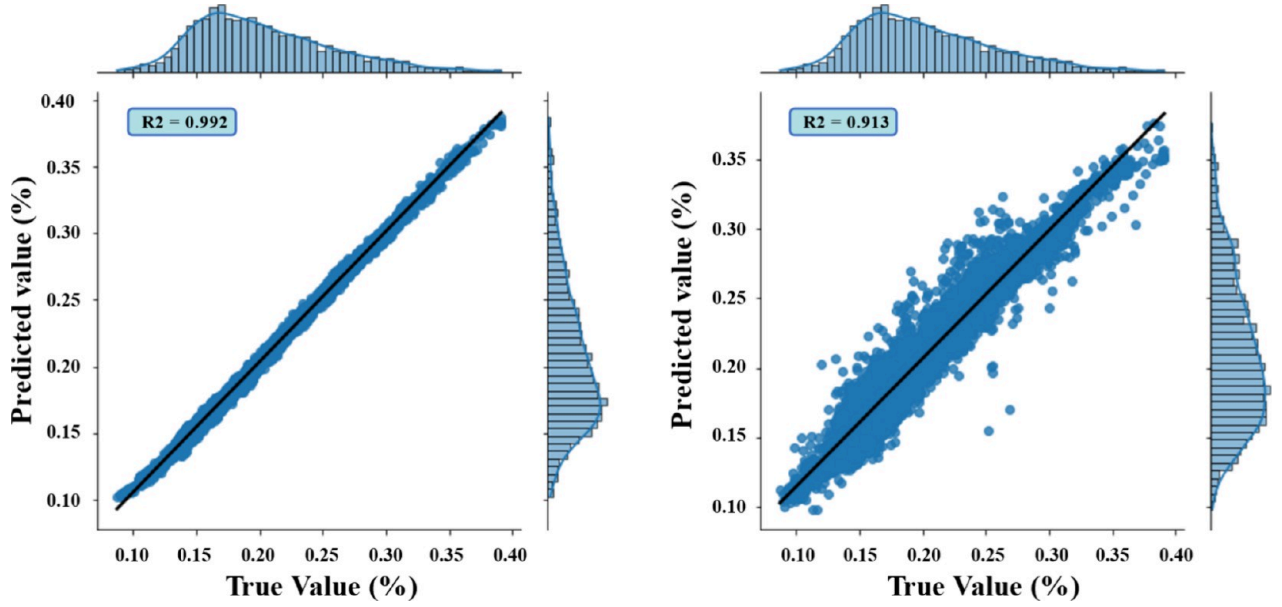

Figure 12. Prediction of porosity against actual labels from (left) binary and (right) grayscale images of Leopard sandstone using Model C.

δ was set to 0.5 in this study. The "Adam"[59] optimizer was used in this experiment to update the network parameters (weights and biases). The Adam optimizer updates the learning rate for each network weight individually, and it takes less time to compute and requires fewer parameters for tuning.

$$\text{Huber Loss} = \begin{cases} \frac{1}{2}(y_i - \hat{y}_i)^2 \text{ for } |y_i - \hat{y}_i| \le \delta \\ \delta\left(|y_i - \hat{y}_i| - \frac{1}{2}\delta\right) \text{ for } |y_i - \hat{y}_i| > \delta \end{cases} \quad (2)$$

where $\hat{y}_i$ is the true value; y_i is the predicted value; and δ is the hyperparameter.

The data set was too large to be processed in a single batch, so it was divided into smaller batches (240 images each) to train the model. We set optimal values for the learning rate through manual adjustment to optimize the individual model accuracy and computational speed. The learning rate was set to 1×10^{-6} while training the model for predicting porosity and pore surface area, and for throat area, it was set to 1×10^{-4}. The "TensorFlow"[60] platform was used to train the network in this work. Google Colaboratory was used to run the code, and each step was processed in around 26 s using a Tesla T4 GPU.

3.3.2. Regression Models for Permeability Prediction. The morphological descriptors and absolute permeability of each of the subdivided ROIs (200 × 200 × 200) of Bentheimer sandstone were used to construct proxy models using four different machine learning algorithms: random forest (RF), multilayer perceptron (MLP), gradient boosting (GBoost), and extreme gradient boosting (XGBoost). The best algorithm was then selected to develop a combined model for predicting an unknown rock's permeability (Leopard sandstone in this study). After that, three models were trained with two different rock samples: the first with the morphological properties, of Bentheimer, the second with only Castlegate properties, and the third with combined Bentheimer and Castlegate properties. We used 80% of the data set to train the model while allocating the remaining 20% to validate the model's performance. Log transformation was applied to reduce the skewness of the data set, and GridSearchCV was used to find the best hyperparameters for the model by optimizing for the minimum mean squared error. Metrics such as mean squared error (MSE), mean absolute error (MAE), root mean squared error (RMSE), and *R*-square score were computed to evaluate the model.

https://doi.org/10.1021/acsomega.3c10131
ACS Omega 2024, 9, 30205−30223

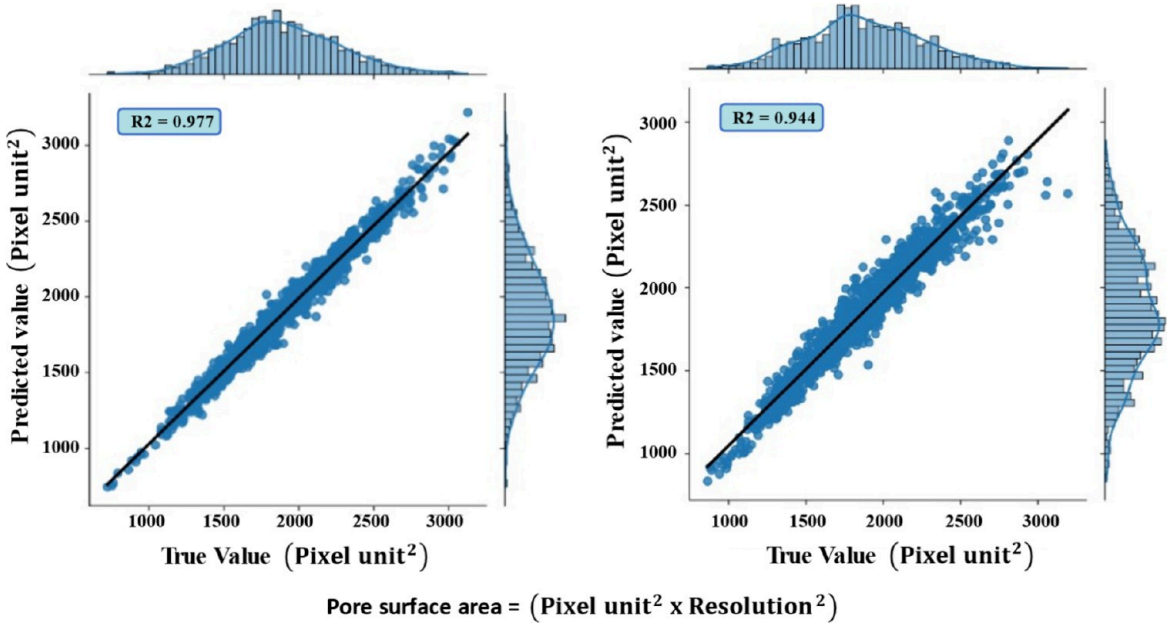

Figure 13. Prediction of pore surface area (PSA) against actual labels from (left) binary and (right) grayscale images of Leopard sandstone using Model C.

4. RESULTS AND DISCUSSION

This section presents training, validation, and testing results for predicting the morphological properties and permeability of a rock sample using CNN and regression models, respectively. The CNN estimation accuracy increases with every elapsed epoch. Various metrics have been used to evaluate the model such as mean absolute percentage error (MAPE), mean squared percentage error (MSPE), and root mean squared percentage error (RMSPE). Table 4 shows the evaluation metrics calculated for Model A, Model B, and Model C. Model A was trained, validated, and tested using the Bentheimer sandstone images, Model B with Castlegate images, and Model C with Bentheimer and Castlegate images combined.

Next, we used these trained models (Model A, Model B, and Model C) to predict the morphological descriptors of an unknown rock (Leopard sandstone) that the models do not see.

4.1. Porosity (Ø). Figure 12 shows the porosity predictions with binary and grayscale images against the test data set generated from Leopard sandstone using Model C. The model was trained for 200 epochs, after which the average error loss stays constant (Figure 21). The performance of Model C in predicting porosity from binary and grayscale images demonstrates a significant improvement compared to the results reported in other literature.[61] This improvement can be attributed to several factors, such as image preprocessing, data cleaning, and the CNN model architecture used in this study. The *R*-squared (R^2) metric in Model C achieved 0.992 for predicting porosity with binary images and 0.913 for predicting porosity with grayscale images. Furthermore, when employing Model C, the MAPE for porosity prediction of Leopard sandstone stands at 2.19% with binary images and at 6.25% for grayscale images, which marks a notable improvement compared to the porosity prediction from Model A and Model B. Model A resulted in the errors (MAPE) of 16.19% for binary images and 19.91% for grayscale images, whereas Model B showed errors of 2.32% with binary images and 6.59% with grayscale images. This result shows that the pore network and other morphological characteristics of the Castlegate rock are similar to those of the Leopard sandstone, which is further discussed in Section 4.4.

4.2. Pore Surface Area (PSA). Model C was trained for 300 epochs to predict the pore surface area (PSA) of Leopard sandstone (Figure 22). The R^2 score for predicting PSA using Model C is 0.977 and 0.944 for the binary and grayscale images, respectively (Figure 13). The MAPE for predicting the PSA of Leopard sandstone utilizing Model C is 3.04% for binary images and 8.35% for grayscale images. The MAPE to predict the PSA of Leopard sandstone using Model A is much higher than those using Model B and Model C, 6.52% and 9.56% for binary and grayscale images, respectively. For Model B, the error (MAPE) is 3.6%, and 9.45% is the value for binary and grayscale images, respectively.

4.3. Throat Area (TA). The pore throat area computed from the Gostick algorithm (Section 3.2.2) was positively skewed, with a significant number of calculated values larger than 280 μm. The mean of the throat area was 133.9 μm, with a standard deviation of 56.1 μm. The skewness in training data can negatively impact the predictive ability of an ML model. Hence, we applied the log transformation method to reduce the skewness, after which the mean of the throat area became 4.82 μm, with a standard deviation of 0.43. The log transformation is a mathematical operation that reduces skewness and compresses large values while expanding smaller ones. It involves taking the logarithm of the original values, which results in a new set of values that are proportional to the original values but with a more manageable range of variations. Mathematically, the log transformation can be presented as eq 3.

$$y = \log(x) \tag{3}$$

where x is the original value, and y is the transformed value.

Figure 14 illustrates the distribution and probability plot changes of the TA after the log transformation. The red line in the normal probability plot represents the expected values of a standard normal distribution, which is used to compare the distribution of the transformed variable against a normal distribution. Although the skewness of the training data

https://doi.org/10.1021/acsomega.3c10131
ACS Omega 2024, 9, 30205−30223

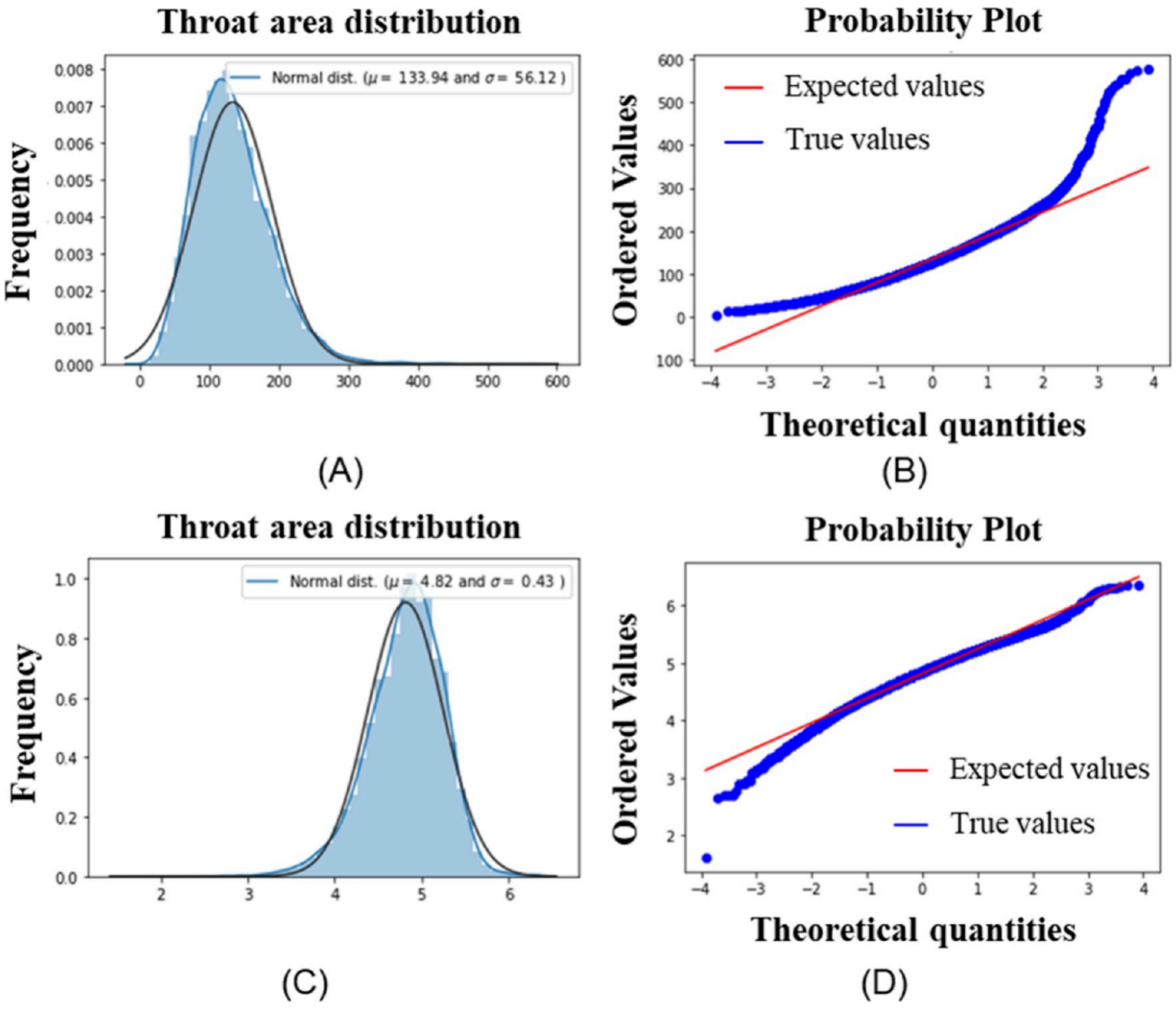

Figure 14. Distribution and probability plot of the throat area (A, B) before log transformation and (C, D) after log transformation.

decreases after transformation, the data becomes slightly negatively skewed.

Figure 15 presents the prediction of TA from binary and grayscale images of Leopard sandstone with Model C after 300 epochs (Figure 23). The R^2 values for TA prediction using binary and grayscale images of Leopard sandstone are 0.776 and 0.744, respectively. Model B results in a MAPE of 6.08% for binary images and 6.37% for grayscale images when applied to the Leopard sandstone. However, Model A results in higher MAPE values: 7.34% for binary images and 7.4% for grayscale images. Also, with Model B, the MAPE is higher than that of Model C, with 6.74% and 10.04% for grayscale and binary images, respectively.

Overall, it is observed, in terms of predicting Leopard sandstone properties, that Model B outperforms Model A, indicating the similarity between Castlegate and Leopard morphological properties. However, overall, the combined model (Model C) trained with both Bentheimer and Castlegate sandstone exhibits higher accuracy in predicting Leopard sandstone's morphological properties, indicating the importance of diverse training data for robust model performance.

4.4. Permeability Prediction. The permeability prediction from digital rock images using CNN, which we previously used for the porosity prediction, is significantly complicated and resource-intensive. The permeability prediction based on CNN requires complex architecture and significant computational resources, which may not be tenable if a large number of samples are to be analyzed. Hence, we used a data-driven method that is significantly easier and more efficient to implement than image-based approaches.

The morphological properties extracted from Bentheimer sandstone were trained with four different algorithms (XGboost, GBoost, RF, and MLP). Eighty percent of the data set of Bentheimer properties was used for training and 20 percent for testing. Among other models, the XGboost demonstrated the best accuracy for predicting the permeability of the Bentheimer sandstone, achieving an R^2 score of 0.934. Figure 16 shows the permeability prediction of Bentheimer sandstone blocks against the LBM simulation results using the XGBoost model. The XGboost provides the best accuracy among the tested models as it can handle complex relationships between features in the data. It also includes L1 and L2 regularization terms, which help

https://doi.org/10.1021/acsomega.3c10131
ACS Omega 2024, 9, 30205−30223

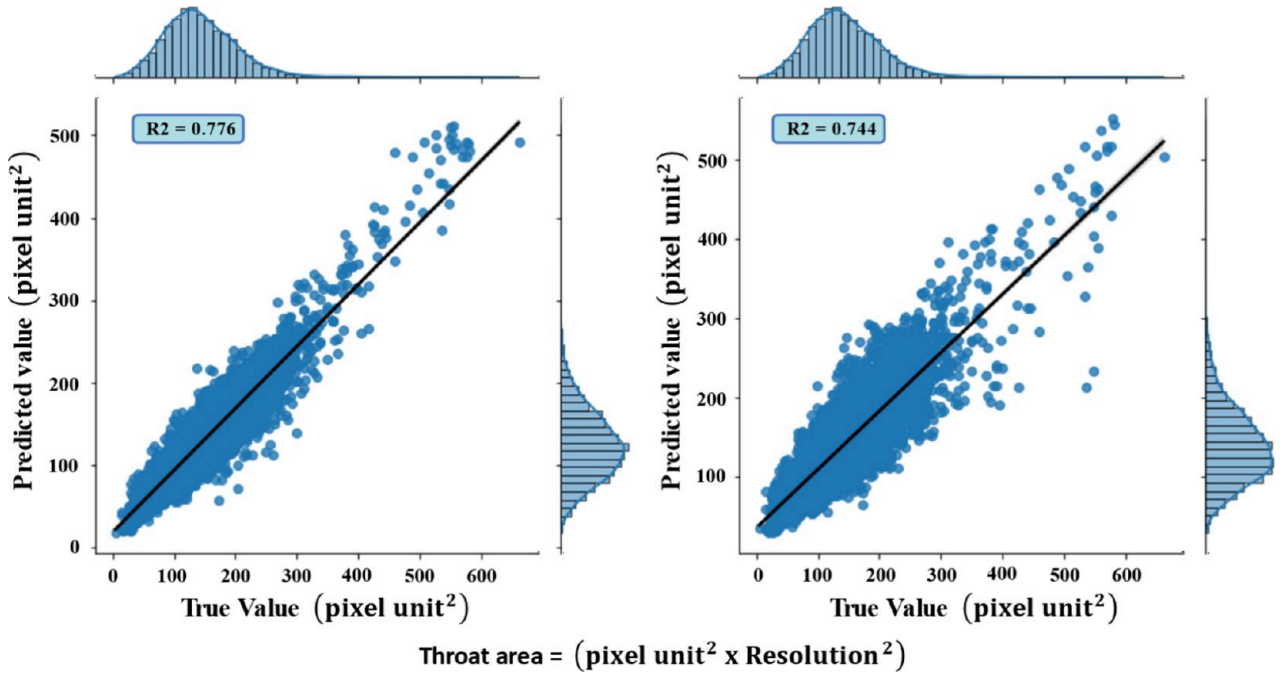

Figure 15. Prediction of throat area against actual labels from (left) binary and (right) grayscale images of Leopard sandstone using Model C.

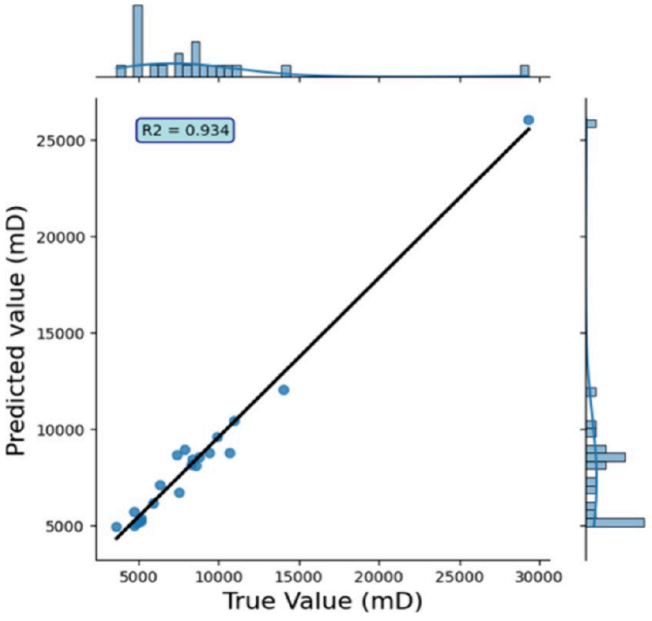

Figure 16. Comparison between targets and predictions for predicting Bentheimer sandstone permeability with the XGBoost model.

prevent overfitting and make the model more robust.[62] However, in this study, the MLP model becomes less accurate for predicting the permeability. Table 5 shows the values of the evaluation matrices for different models (XGBoost, GBoost, RF, and MLP).

Next, three different models were trained using Bentheimer and Castlegate rock samples with XGboost to predict the permeability of an unknown rock sample (Leopard). The first two models were trained on the morphological properties of individual rock samples, and the third model was trained on the properties of both Bentheimer and Castlegate sandstones.

Each model resulted in an acceptable accuracy for permeability prediction when tested with the same rock sample.

Table 5. Comparison between Different Evaluation Functions for the Models Used for Predicting Permeability

Evaluation functions	XGBoost	GBoost	RF	MLP
MAE	0.087	0.117	0.158	0.217
MSE	0.013	0.018	0.051	0.117
RMSE	0.114	0.136	0.227	0.342
R^2 score	0.933	0.906	0.738	0.407

However, when the models were tested with Leopard sandstone, the model trained with the combined properties of Bentheimer and Castlegate sandstone provided the most accurate results. The MAE, RMSE, and R^2 for permeability prediction of Leopard sandstone using all the models are summarized in Table 6.

Table 6. R^2, MAE, and RMSE Errors for Predicting the Permeability of Leopard Sandstone Using Models Trained on Three Distinct Datasets

Sandstone Properties for model training	MAE	RSME	R^2
Bentheimer	0.112	0.146	0.466
Castlegate	0.069	0.105	0.710
Bentheimer and Castlegate	0.049	0.084	0.813

Across all of the metrics, the combined model delivers significantly improved rock property prediction. The improvement is more apparent when comparing the combined model to the model trained with just the Bentheimer sandstone. However, we observe improvement in prediction even for the combined model compared with the model trained with the Castlegate sandstone.

The improvement in accuracy for the combined model was also observed in predicting the morphological properties (Sections 4.1−4.3). Figure 17 illustrates the accuracy in the prediction of Leopard sandstone permeability with models trained with different data sets.

Feature importance analysis was conducted to understand the critical parameters influencing the permeability prediction of the

https://doi.org/10.1021/acsomega.3c10131
ACS Omega 2024, 9, 30205−30223

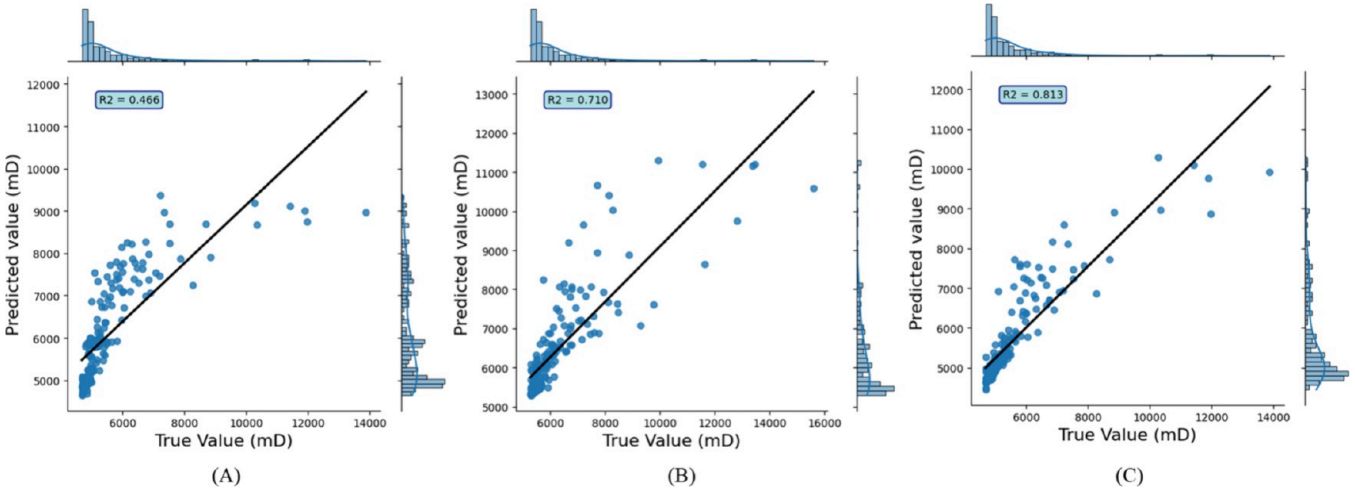

Figure 17. Prediction of permeability of Leopard sandstone with models trained with (A) Bentheimer sandstone properties, (B) Castlegate sandstone properties, and (C) Bentheimer and Castlegate sandstone properties.

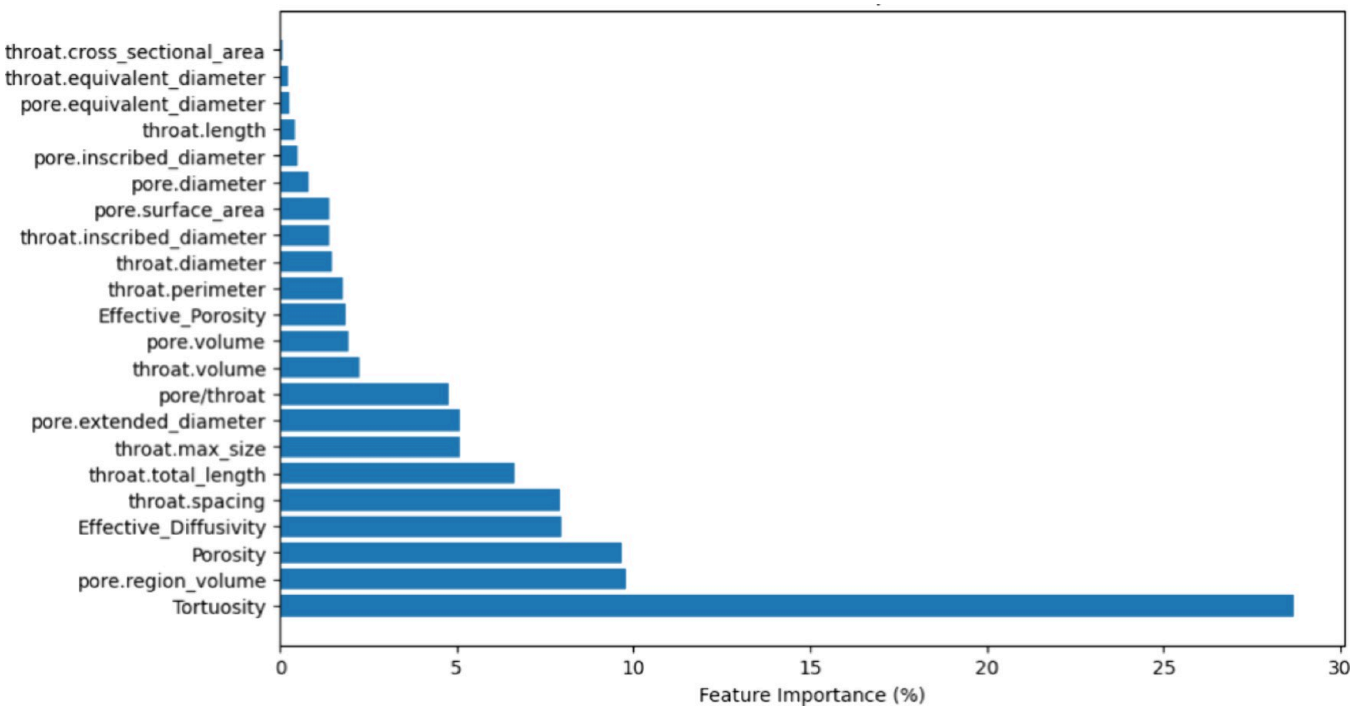

Figure 18. Feature importance plot for permeability prediction, based on the XGBoost model trained with the combined properties of Bentheimer and Castlegate sandstone.

rock samples. Previous studies reported that morphological properties like porosity, tortuosity, and pore-to-throat ratio correlate with the porous media's permeability.[63−65] Our findings underscore the paramount role of tortuosity, which emerged as the most significant factor with an importance percentage of ∼28%, indicating the complexity of fluid paths within the rock as a crucial determinant of permeability. Additionally, porosity and pore region volume were identified as important features with importance percentages of ∼9%, highlighting the significance of void spaces within the rock for fluid storage and transmissibility. The analysis also revealed the importance of effective diffusivity in influencing permeability (∼8%), pointing toward the relevance of fluid movement ease between connecting pores. Figure 18 shows the feature importance plot for permeability prediction using the data-driven model with morphological properties.

In order to understand the reason for the improved prediction of both morphological properties and permeability using the individually trained model trained with Castlegate sandstone, we analyzed the underlying pore-scale properties of each rock, which showed that the statistical distributions of features in the Castlegate sandstone are closer to those of Leopard sandstone. The key features such as pore region volume, porosity, pore/throat ratio, effective diffusivity, and tortuosity in Castlegate sandstone share mean values and distributions that align more closely with those in Leopard sandstone, which are critical in defining permeability. Figure 19 shows the box plot for various features used for training the machine learning model, and the

https://doi.org/10.1021/acsomega.3c10131
ACS Omega 2024, 9, 30205−30223

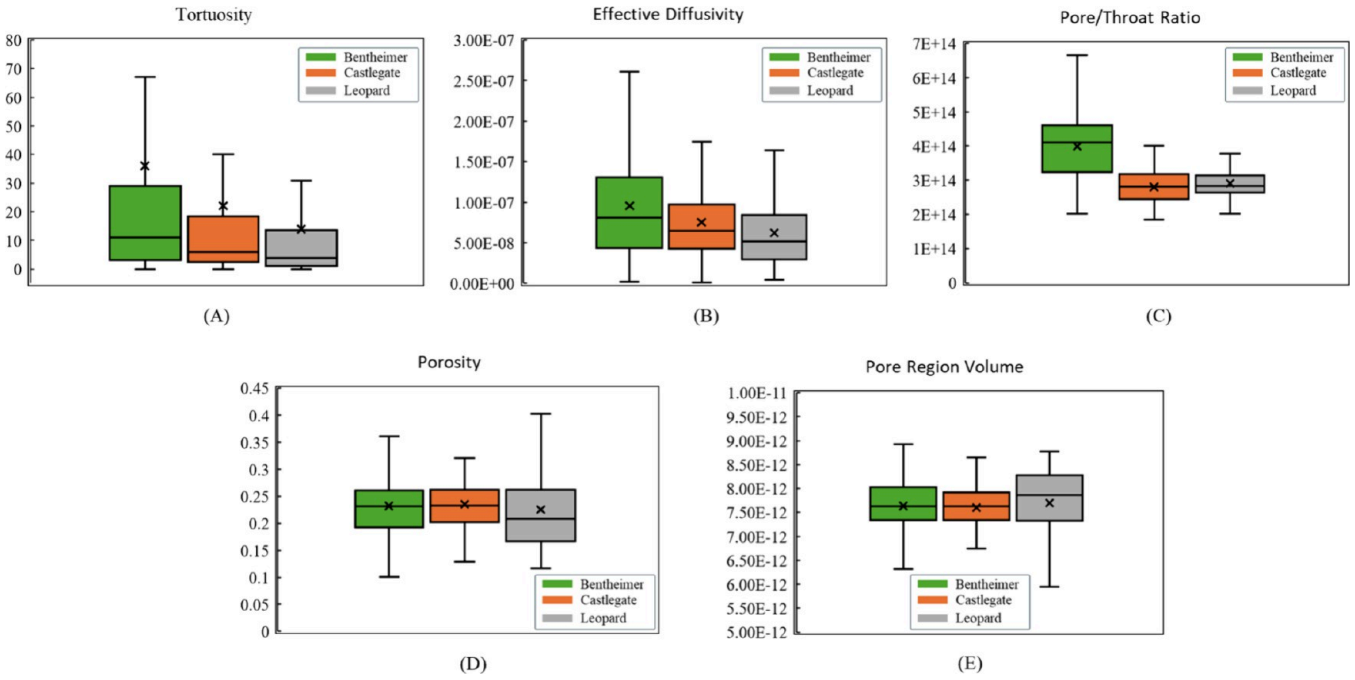

Figure 19. Box plot showing the key features for Castlegate, Bentheimer, and Leopard sandstones. The morphological properties of Castlegate sandstone are significantly similar to those of Leopard sandstone.

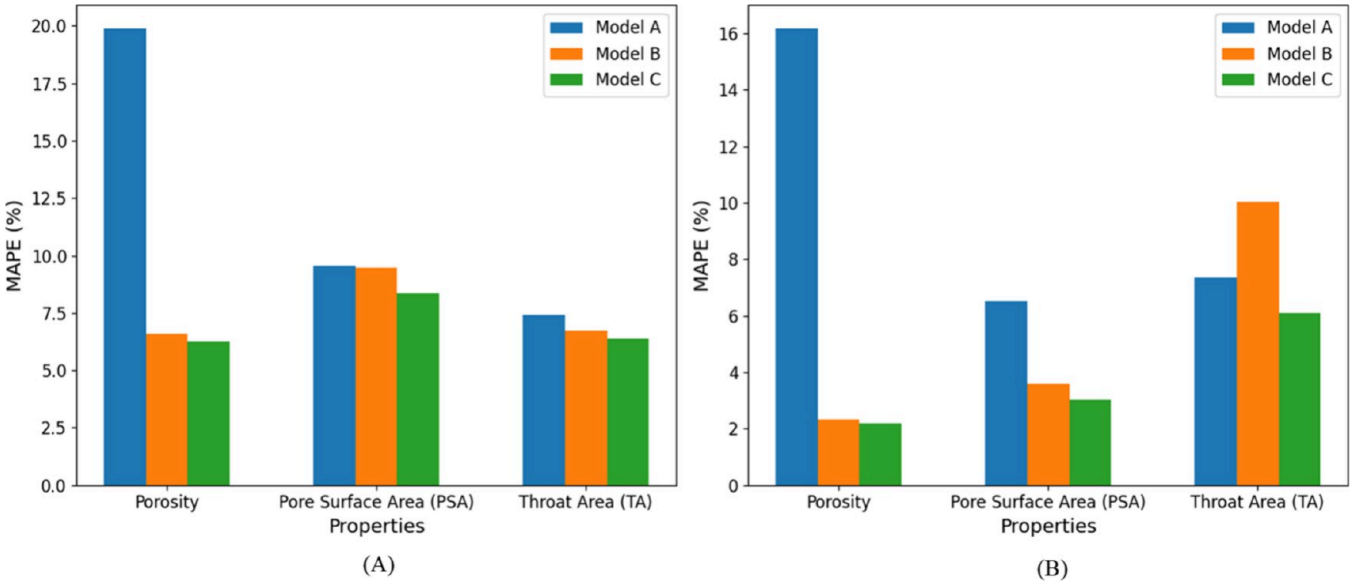

Figure 20. MAPE for predicting properties (Ø, PSA, and TA) of Leopard sandstone by using (A) grayscale images and (B) binary images.

descriptive statistics of these features are summarized in Appendix, Table 7.

5. SUMMARY AND CONCLUSIONS

This study proposed a workflow to predict the morphological properties of an unknown rock sample using micro-CT images, which can later be used to predict the permeability of the porous media. Various flow properties, including porosity and permeability, can be extracted by using the proposed workflow without extensive laboratory experiments. These flow properties are crucial in modeling the flow in porous media. This work used Leopard sandstone as an unknown rock sample to predict morphological properties (Ø, TA, and PSA). Three distinct models were trained using two distinct rock samples: one model only used the images of Bentheimer sandstone (Model A); another one was with only Castlegate sandstone images (Model B); and the last one was with both Bentheimer and Castlegate sandstone images (Model C). The training of Model C required an average duration of 2.5 h, utilizing the Tesla T4 GPU offered by Google Colaboratory. The number of epochs to train the models was selected based on the training and validation loss. Training and validation losses decreased with each additional epoch. Figure 20 summarizes the MAPE for predicting various morphological properties for an unknown rock sample.

In the case of Model C while using grayscale images to predict the properties of Leopard sandstone, the MAPE is 6.25% for porosity, 8.35% for pore surface area, and 6.37% for throat area (Figure 20). On the other hand, while using binary images, the

https://doi.org/10.1021/acsomega.3c10131
ACS Omega 2024, 9, 30205−30223

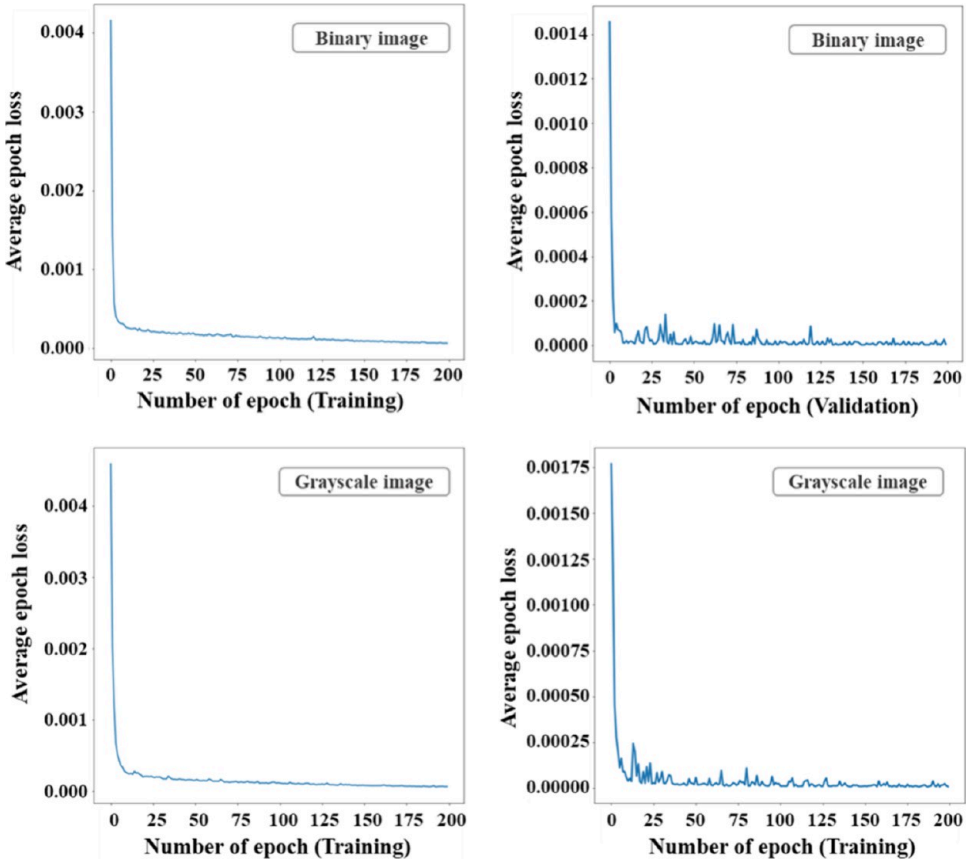

Figure 21. Average error loss during training and validation of Model C to predict porosity.

MAPE is lower: 2.19%, 3.04%, and 6.08% for predicting porosity, pore surface area, and throat area, respectively (Figure 20). This is because the model generated with grayscale images is more sensitive to noise and defects, resulting in a higher prediction error than the model developed with binary images.[66] Accurate rock image segmentation is essential for extracting the precise properties of the rock sample. This study applied two different segmentation methods, the U-Net model and the Otsu thresholding method, to extract the properties. Then, the segmented images were evaluated against the manually segmented images. The results show that with proper data preprocessing Otsu thresholding can provide satisfactory segmentation results and improve model accuracy. We found that deleting the defective images and reducing skewness reduced the MAPE of property prediction by around 3%. Furthermore, this study also shows that it is possible to create an enhanced model trained from a large variety of rock samples to predict the accurate morphological descriptors of an unknown rock sample. The workflow can also be applied to predict other morphological properties using high-resolution micro-CT images. To validate the workflow presented in this study, the average pore size was calculated from the extracted network of the rock images and trained with the proposed CNN model (Model C). Previous studies have indicated that model accuracy tends to be lower when predicting properties extracted from the pore network.[61] However, the results show that the proposed model (Model C) provides good accuracy in predicting the average pore size of an unknown rock sample (Leopard sandstone), with an R^2 value of 0.91 and 0.94 for grayscale and binary images, respectively.

We also demonstrated a data-driven workflow for predicting the permeability of porous media using various morphological data extracted from the rock sample. The XGboost model resulted in the most accurate prediction of permeability for an unknown rock sample. The model trained with Castlegate sandstone outperformed the model trained with the Bentheimer sandstone data set in terms of predicting both the morphological property and permeability of the Leopard sandstone, which indicates the similarity between Castlegate and Leopard sandstone. The feature importance analysis revealed that the statistical distributions of key features in the Castlegate sandstone are closer to those of Leopard sandstone (Figure 19). For predicting the permeability of Leopard sandstone, the models trained using Bentheimer and Castlegate sandstone properties yielded R^2 values of 0.466 and 0.710, respectively (Figure 17). However, the combined model (trained with both Bentheimer and Castlegate sandstone) was more accurate in predicting the properties of Leopard sandstone, indicating the importance of diverse training data for robust model performance. The R^2 value for predicting the permeability of Leopard sandstone was 0.813 by using the model that is trained with both Bentheimer and Castlegate sandstone properties.

The model presented in this work for predicting the morphological descriptors of porous media still has room for improvement. Methods like the generative adversarial network (GAN)[66] and hybrid stochastic deep-learning (HSDL)[67] can be applied to increase the image resolution and thus increase the prediction accuracy. In addition, the hyperparameters of the CNN model can also be tuned for better model performance. For the models in this study, the decrease in the learning rate and increase in the number of epochs improved the property

https://doi.org/10.1021/acsomega.3c10131
ACS Omega 2024, 9, 30205−30223

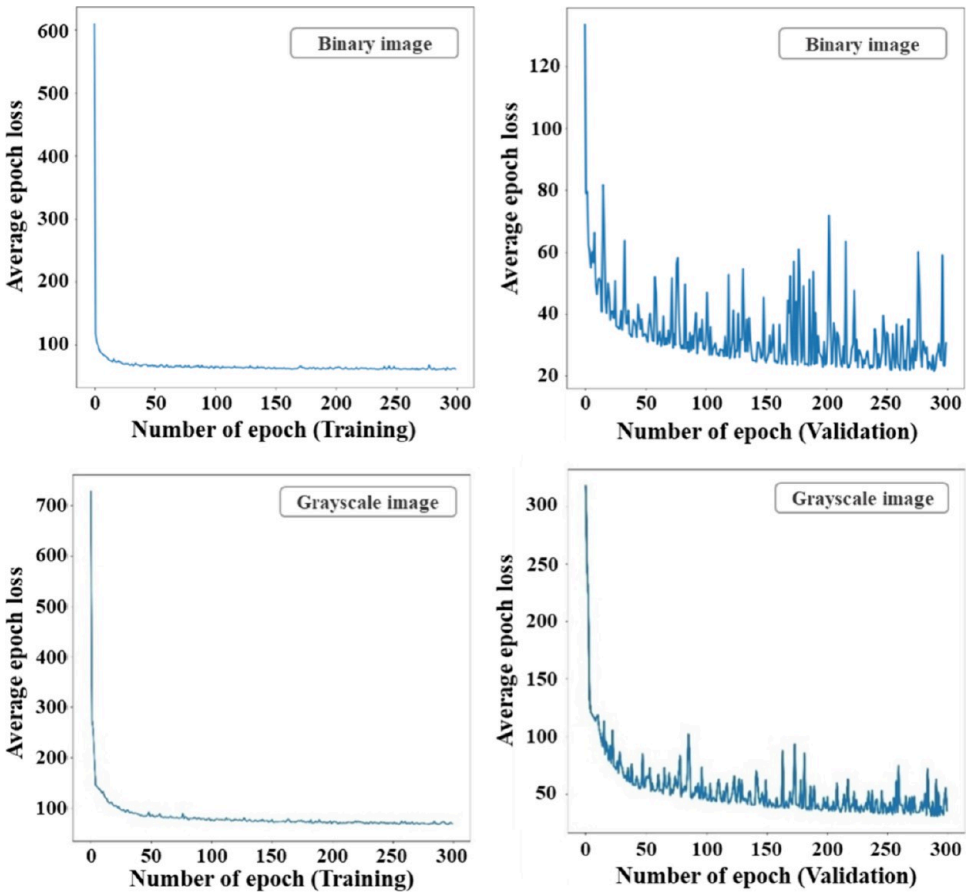

Figure 22. Average error loss during training and validation of Model C to predict pore surface area.

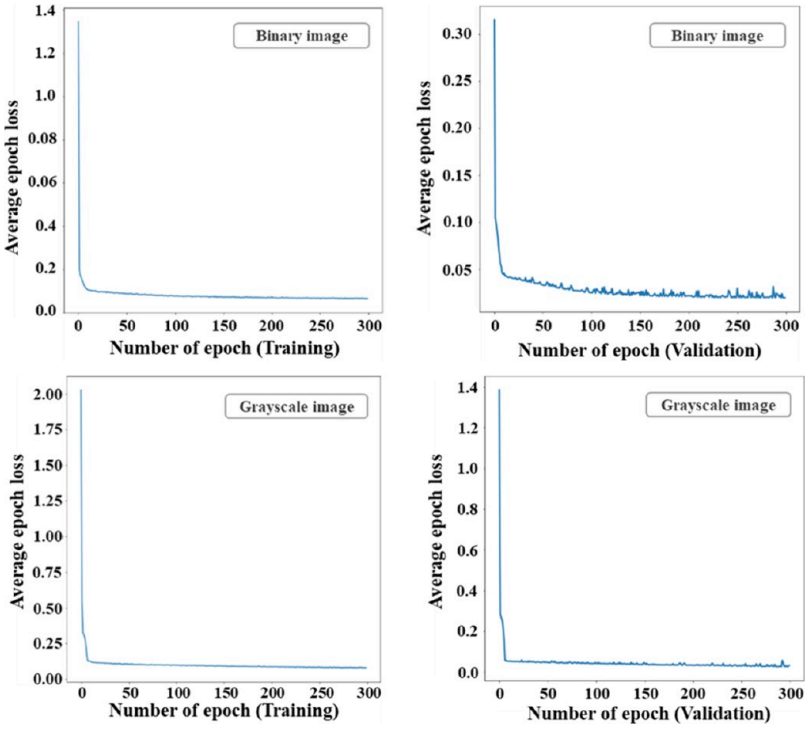

Figure 23. Average error loss during training and validation of Model C to predict throat area.

prediction with grayscale images. The MAPE while training Model A with grayscale images for porosity prediction decreased from 24.60% with a learning rate of 1×10^{-3} to 1.43% when the learning rate was 1×10^{-6}. Future studies will focus on

https://doi.org/10.1021/acsomega.3c10131
ACS Omega 2024, 9, 30205−30223

Table 7. Descriptive Statistics of Key Features of Castlegate, Bentheimer, and Leopard Sandstone Subdivided Blocks for Machine Learning Model Training

	Bentheimer Sandstone				
	Tortuosity	Effective Diffusivity	Pore/Throat	Porosity	Pore Region Volume
min	7.51×10^{-03}	2.11×10^{-09}	2.02×10^{14}	0.10	6.32×10^{-12}
25%	3.21×10^{00}	4.36×10^{-08}	3.24×10^{14}	0.19	7.35×10^{-12}
Median	1.10×10^{01}	8.07×10^{-08}	4.11×10^{14}	0.23	7.64×10^{-12}
75%	2.91×10^{01}	1.31×10^{-07}	4.61×10^{14}	0.26	8.03×10^{-12}
Mean	3.60×10^{01}	9.55×10^{-08}	3.99×10^{14}	0.23	7.63×10^{-12}
max	6.70×10^{01}	2.62×10^{-07}	6.66×10^{14}	0.36	8.93×10^{-12}
	Castlegate Sandstone				
	Tortuosity	Effective Diffusivity	Pore/Throat	Porosity	Pore Region Volume
min	8.31×10^{-03}	1.11×10^{-09}	1.85×10^{14}	0.12	6.75×10^{-12}
25%	2.50×10^{00}	4.29×10^{-08}	2.45×10^{14}	0.20	7.34×10^{-12}
Median	5.97×10^{00}	6.44×10^{-08}	2.81×10^{14}	0.23	7.63×10^{-12}
75%	1.84×10^{01}	9.76×10^{-08}	3.18×10^{14}	0.26	7.93×10^{-12}
Mean	2.21×10^{01}	7.54×10^{-08}	2.80×10^{14}	0.23	7.60×10^{-12}
max	4.01×10^{01}	1.80×10^{-07}	4.00×10^{14}	0.32	8.60×10^{-12}
	Leopard Sandstone				
	Tortuosity	Effective Diffusivity	Pore/Throat	Porosity	Pore Region Volume
min	1.58×10^{-02}	4.02×10^{-09}	2.03×10^{14}	0.11	5.95×10^{-12}
25%	1.13×10^{00}	2.95×10^{-08}	2.64×10^{14}	0.16	7.33×10^{-12}
Median	3.77×10^{00}	5.17×10^{-08}	2.84×10^{14}	0.20	7.87×10^{-12}
75%	1.35×10^{01}	8.44×10^{-08}	3.15×10^{14}	0.26	8.28×10^{-12}
Mean	1.39×10^{01}	6.22×10^{-08}	2.91×10^{14}	0.22	7.70×10^{-12}
max	3.10×10^{01}	1.64×10^{-07}	3.77×10^{14}	0.40	8.77×10^{-12}

improving the predictive power of the proposed model using other advanced algorithms and tuning different hyperparameters.

6. APPENDIX

The average error loss during the training and validation for predicting porosity, pore surface area, and throat area using Model C is presented in Figures 21, 22, and 23.

AUTHOR INFORMATION

Corresponding Author

Aaditya Khanal − *The Jasper Department of Chemical Engineering, The University of Texas at Tyler, Tyler, Texas 75799, United States; Russell School of Chemical Engineering and McDougall School of Petroleum Engineering, The University of Tulsa, Tulsa, Oklahoma 74104, United States;* orcid.org/0000-0003-1333-7457; Email: aadityakhanal@uttyler.edu, aadityakhanal@gmail.com

Author

Md Irfan Khan − *The Jasper Department of Chemical Engineering, The University of Texas at Tyler, Tyler, Texas 75799, United States;* orcid.org/0000-0001-9790-7386

Complete contact information is available at: https://pubs.acs.org/10.1021/acsomega.3c10131

Notes

The authors declare no competing financial interest.

ACKNOWLEDGMENTS

We thank the anonymous reviewers for their edits and suggestions, which improved our manuscript. This material is based upon work supported partly by the American Chemical Society Petroleum Research Fund (PRF # 62679-UNI9) and partly by the National Science Foundation Award under CBET-2245484. Any opinions, findings, conclusions, or recommendations expressed in this material are those of the author(s) and do not necessarily reflect the views of the funding agencies.

TABLE OF ABBREVIATIONS

CNN, Convolutional neural network
2D, Two dimensional
3D, Three dimensional
Micro-CT, Microcomputed tomography
RCA, Routine core analysis
SCAL, Special core analysis
ML, Machine learning
ANN, Artificial neural network
Ø, Porosity
PSA, Pore surface area
TA, Throat area
ROI, Region of interest
ReLU, Rectified linear unit
MAE, Mean absolute error
MSE, Mean squared error
MAPE, Mean absolute percentage error
MSPE, Mean squared percentage error
RMSPE, Root mean squared percentage error
GAN, Generative adversarial network
HSDL, Hybrid stochastic deep learning
XGBoost, Extreme gradient boost
GBoost, Gradient boost
RF, Random forest
MLP, Multilayer perceptron

https://doi.org/10.1021/acsomega.3c10131
ACS Omega 2024, 9, 30205−30223

REFERENCES

(1) Khanal, A.; Weijermars, R. Comparison of Flow Solutions for Naturally Fractured Reservoirs Using Complex Analysis Methods (CAM) and Embedded Discrete Fracture Models (EDFM): Fundamental Design Differences and Improved Scaling Method. *Geofluids.* **2020**, *2020*, 1−20.

(2) Khanal, A.; Irfan Khan, M.; Fahim Shahriar, M. Comprehensive parametric study of CO2 sequestration in deep saline aquifers. *Chem. Eng. Sci.* **2024**, *287*, No. 119734.

(3) Khanal, A.; Shahriar, M. F. Physics-Based Proxy Modeling of CO2 Sequestration in Deep Saline Aquifers. *Energies.* **2022**, *15*, 4350.

(4) Bachu, S.; Bonijoly, D.; Bradshaw, J.; Burruss, R.; Holloway, S.; Christensen, N. P.; Mathiassen, O. M. CO2 storage capacity estimation: Methodology and gaps. *Int. J. Greenh. Gas Control.* **2007**, *1*, 430−443.

(5) S. Edition, Recommended practices for core analysis. *API Recomm. Pract.* **1998**.

(6) McPhee, C.; Reed, J.; Zubizarreta, I. Best Practice in Coring and Core Analysis. *Core Analysis - A Best Practice Guide* **2015**, *64*, 1−15.

(7) Berg, C. F.; Lopez, O.; Berland, H. Industrial applications of digital rock technology. *J. Pet. Sci. Eng.* **2017**, *157*, 131−147.

(8) Amabeoku, M. O.; BinNasser, R. H. Quality Control/Quality Assurance Assessments of Core Analysis Data from Multiple Commercial Laboratories. *All Days, SPE* **2012**, 605−616.

(9) Alpak, F. O.; Berg, S.; Zacharoudiou, I. Prediction of fluid topology and relative permeability in imbibition in sandstone rock by direct numerical simulation. *Adv. Water Resour.* **2018**, *122*, 49−59.

(10) Iraji, S.; Soltanmohammadi, R.; Munoz, E. R.; Basso, M.; Vidal, A. C. Core scale investigation of fluid flow in the heterogeneous porous media based on X-ray computed tomography images: Upscaling and history matching approaches. *Geoenergy Sci. Eng.* **2023**, *225*, No. 211716.

(11) Malki, M. L.; Saberi, M. R.; Kolawole, O.; Rasouli, V.; Sennaoui, B.; Ozotta, O. Underlying mechanisms and controlling factors of carbonate reservoir characterization from rock physics perspective: A comprehensive review. *Geoenergy Sci. Eng.* **2023**, *226*, No. 211793.

(12) Dong, H.; Sun, J.; Lin, Z.; Fang, H.; Li, Y.; Cui, L.; Yan, W. 3D pore-type digital rock modeling of natural gas hydrate for permafrost and numerical simulation of electrical properties. *J. Geophys. Eng.* **2018**, *15*, 275−285.

(13) Andrä, H.; Combaret, N.; Dvorkin, J.; Glatt, E.; Han, J.; Kabel, M.; Keehm, Y.; Krzikalla, F.; Lee, M.; Madonna, C.; Marsh, M.; Mukerji, T.; Saenger, E. H.; Sain, R.; Saxena, N.; Ricker, S.; Wiegmann, A.; Zhan, X. Digital rock physics benchmarks—Part I: Imaging and segmentation. *Comput. Geosci.* **2013**, *50*, 25−32.

(14) Niu, Y.; Mostaghimi, P.; Shabaninejad, M.; Swietojanski, P.; Armstrong, R.T. Digital Rock Segmentation for Petrophysical Analysis With Reduced User Bias Using Convolutional Neural Networks. *Water Resour. Res.* **2020**, DOI: 10.1029/2019WR026597.

(15) Karimpouli, S.; Tahmasebi, P. Segmentation of digital rock images using deep convolutional autoencoder networks. *Comput. Geosci.* **2019**, *126*, 142−150.

(16) Wang, H.; Dalton, L.; Fan, M.; Guo, R.; McClure, J.; Crandall, D.; Chen, C. Deep-learning-based workflow for boundary and small target segmentation in digital rock images using UNet++ and IK-EBM. *J. Pet. Sci. Eng.* **2022**, *215*, No. 110596.

(17) Phan, J.; Ruspini, L. C.; Lindseth, F. Automatic segmentation tool for 3D digital rocks by deep learning. *Sci. Rep.* **2021**, *11*, 19123.

(18) Patel, A. K.; Chatterjee, S. Computer vision-based limestone rock-type classification using probabilistic neural network. *Geosci. Front.* **2016**, *7*, 53−60.

(19) Wang, S.; Chen, Z.; Chen, S. Applicability of deep neural networks on production forecasting in Bakken shale reservoirs. *J. Pet. Sci. Eng.* **2019**, *179*, 112−125.

(20) Unrau, S.; Torrione, P.; Hibbard, M.; Smith, R.; Olesen, L.; Watson, J. Machine Learning Algorithms Applied to Detection of Well Control Events. In *SPE-188104-MS*, 2017. DOI: 10.2118/188104-MS.

(21) Jha, H. S.; Khanal, A.; Seikh, H. M. D.; Lee, W. J. A comparative study on outlier detection techniques for noisy production data from unconventional shale reservoirs. *J. Nat. Gas Sci. Eng.* **2022**, *105*, No. 104720.

(22) Ebadi, M.; Armstrong, R. T.; Mostaghimi, P.; Wang, Y. D.; Alqahtani, N.; Amirian, T.; James, L. A.; Parmar, A.; Zahra, D.; Hamze, H.; Koroteev, D. Predictive Soft Computing Methods for Building Digital Rock Models Verified by Positron Emission Tomography Experiments. *Water Resour. Res.* **2022**, DOI: 10.1029/2021WR031814.

(23) Tembely, M.; AlSumaiti, A. Deep Learning for a Fast and Accurate Prediction of Complex Carbonate Rock Permeability From 3D Micro-CT Images. In *SPE-197457-MS*, 2019. DOI: 10.2118/197457-MS.

(24) van der Linden, J. H.; Narsilio, G. A.; Tordesillas, A. Machine learning framework for analysis of transport through complex networks in porous, granular media: A focus on permeability. *Phys. Rev. E* **2016**, *94*, 022904.

(25) Tang, M.; Liu, Y.; Durlofsky, L. J. A deep-learning-based surrogate model for data assimilation in dynamic subsurface flow problems. *J. Comput. Phys.* **2020**, *413*, No. 109456.

(26) Tian, J.; Qi, C.; Sun, Y.; Yaseen, Z. M.; Pham, B. T. Permeability prediction of porous media using a combination of computational fluid dynamics and hybrid machine learning methods. *Eng. Comput.* **2021**, *37*, 3455.

(27) Tembely, M.; AlSumaiti, A. M.; Alameri, W. S. Machine and deep learning for estimating the permeability of complex carbonate rock from X-ray micro-computed tomography. *Energy Reports.* **2021**, *7*, 1460−1472.

(28) Tian, J.; Qi, C.; Sun, Y.; Yaseen, Z. M. Surrogate permeability modelling of low-permeable rocks using convolutional neural networks. *Comput. Methods Appl. Mech. Eng.* **2020**, *366*, No. 113103.

(29) Kamrava, S.; Tahmasebi, P.; Sahimi, M. Linking Morphology of Porous Media to Their Macroscopic Permeability by Deep Learning. *Transp. Porous Media.* **2020**, *131*, 427−448.

(30) Hong, J.; Liu, J. Rapid estimation of permeability from digital rock using 3D convolutional neural network. *Comput. Geosci.* **2020**, *24*, 1523−1539.

(31) Takbiri, S.; Kazemi, M.; Takbiri-Borujeni, A.; McIlvain, J. A deep learning approach to predicting permeability of porous media. *J. Pet. Sci. Eng.* **2022**, *211*, No. 110069.

(32) Wang, H.; Yin, Y.; Hui, X. Y.; Bai, J. Q.; Qu, Z. G. Prediction of effective diffusivity of porous media using deep learning method based on sample structure information self-amplification. *Energy AI.* **2020**, *2*, No. 100035.

(33) Zhou, X.-H.; McClure, J. E.; Chen, C.; Xiao, H. Neural network−based pore flow field prediction in porous media using super resolution. *Phys. Rev. Fluids.* **2022**, *7*, No. 074302.

(34) Saxena, N.; Hows, A.; Hofmann, R.; Alpak, F. O.; Freeman, J.; Hunter, S.; Appel, M. Imaging and computational considerations for image computed permeability: Operating envelope of Digital Rock Physics. *Adv. Water Resour.* **2018**, *116*, 127−144.

(35) Fu, J.; Wang, M.; Chen, B.; Wang, J.; Xiao, D.; Luo, M.; Evans, B. A data-driven framework for permeability prediction of natural porous rocks via microstructural characterization and pore-scale simulation. *Eng. Comput.* **2023**, *39*, 3895.

(36) Tian, J.; Qi, C.; Sun, Y.; Yaseen, Z. M.; Pham, B. T. Permeability prediction of porous media using a combination of computational fluid dynamics and hybrid machine learning methods. *Eng. Comput.* **2021**, *37*, 3455−3471.

(37) Houston, A. N.; Otten, W.; Falconer, R.; Monga, O.; Baveye, P. C.; Hapca, S. M. Quantification of the pore size distribution of soils: Assessment of existing software using tomographic and synthetic 3D images. *Geoderma.* **2017**, *299*, 73−82.

(38) Temizel, C.; Odi, U.; Balaji, K.; Aydin, H.; Santos, J. E. Classifying Facies in 3D Digital Rock Images Using Supervised and Unsupervised Approaches. *Energies.* **2022**, *15*, 7660.

(39) Santos, J. E.; Pyrcz, M. J.; Prodanović, M. 3D Dataset of binary images: A collection of synthetically created digital rock images of complex media. *Data Br.* **2022**, *40*, No. 107797.

https://doi.org/10.1021/acsomega.3c10131
ACS Omega 2024, 9, 30205−30223

(40) Willson, C. S.; Lu, N.; Likos, W. J. Quantification of Grain, Pore, and Fluid Microstructure of Unsaturated Sand from X-Ray Computed Tomography Images. *Geotech. Test. J.* **2012**, *35*, No. 20120075.
(41) Al-Bazzaz, W. H.; Al-Mehanna, Y. W. Porosity, Permeability, and MHR Calculations Using SEM and Thin-section Images for Characterizing Complex Mauddud-Burgan Carbonate Reservoir. In *SPE-110730-MS*, 2007. DOI: 10.2118/110730-MS.
(42) Hakimi, M. H.; Shalaby, M. R.; Abdullah, W. H. Diagenetic characteristics and reservoir quality of the Lower Cretaceous Biyadh sandstones at Kharir oilfield in the western central Masila Basin, Yemen. *J. Asian Earth Sci.* **2012**, *51*, 109−120.
(43) Peksa, A. E.; Wolf, K.-H.A.A.; Zitha, P. L. J. Bentheimer sandstone revisited for experimental purposes. *Mar. Pet. Geol.* **2015**, *67*, 701−719.
(44) Cui, I. 3D Sandstone Sample Images. *Digit. Rocks Portal.* **2022**, DOI: 10.17612/FRCM-CN23.
(45) Shikhov, I.; D'Eurydice, M. N.; Arns, J.-Y.; Arns, C. H. An Experimental and Numerical Study of Relative Permeability Estimates Using Spatially Resolved $$T_1$$-z NMR. *Transp. Porous Media.* **2017**, *118*, 225−250.
(46) Sidorenko, M.; Orlov, D.; Ebadi, M.; Koroteev, D. Deep learning in denoising of micro-computed tomography images of rock samples. *Comput. Geosci.* **2021**, *151*, No. 104716.
(47) Huang, T. T. Y.; Jones, A. S.; He, L. H.; Darendeliler, M. A.; Swain, M. V. Characterisation of enamel white spot lesions using X-ray micro-tomography. *J. Dent.* **2007**, *35*, 737−743.
(48) Cankaya, S. A comparative study of some estimation methods for parameters and effects of outliers in simple regression model for research on small ruminants. *Trop. Anim. Health Prod.* **2009**, *41*, 35−41.
(49) Berg, S.; Kutra, D.; Kroeger, T.; Straehle, C. N.; Kausler, B. X.; Haubold, C.; Schiegg, M.; Ales, J.; Beier, T.; Rudy, M.; Eren, K.; Cervantes, J. I.; Xu, B.; Beuttenmueller, F.; Wolny, A.; Zhang, C.; Koethe, U.; Hamprecht, F. A.; Kreshuk, A. ilastik: interactive machine learning for (bio)image analysis. *Nat. Methods.* **2019**, *16*, 1226−1232.
(50) Otsu, N. A Threshold Selection Method from Gray-Level Histograms. *IEEE Trans. Syst. Man. Cybern.* **1979**, *9*, 62−66.
(51) van der Walt, S.; Schönberger, J. L.; Nunez-Iglesias, J.; Boulogne, F.; Warner, J. D.; Yager, N.; Gouillart, E.; Yu, T. scikit-image: image processing in Python. *PeerJ.* **2014**, *2*, No. e453.
(52) Gostick, J. T. Versatile and efficient pore network extraction method using marker-based watershed segmentation. *Phys. Rev. E* **2017**, *96*, No. 023307.
(53) Latt, J.; Malaspinas, O.; Kontaxakis, D.; Parmigiani, A.; Lagrava, D.; Brogi, F.; Belgacem, M. B.; Thorimbert, Y.; Leclaire, S.; Li, S.; Marson, F.; Lemus, J.; Kotsalos, C.; Conradin, R.; Coreixas, C.; Petkantchin, R.; Raynaud, F.; Beny, J.; Chopard, B. Palabos: Parallel Lattice Boltzmann Solver. *Comput. Math. with Appl.* **2021**, *81*, 334−350.
(54) Mohammed Azarudeen, J.; Kaja Bantha Navas, R.; Vikas Reddy, G.; Gowsik Saran, R.S.; Prakash, S.; Anderson, A. Optimizing the process parameters for Powder metallurgy electrode in Electrical Discharge Machining. *Mater. Today Proc.* **2021**, *46*, 9372.
(55) Bear, J.; Bachmat, Y. *Introduction to Modeling of Transport Phenomena in Porous Media*; Springer Netherlands: Dordrecht, 1990. DOI: 10.1007/978-94-009-1926-6.
(56) Lin, G.; Shen, W. Research on convolutional neural network based on improved Relu piecewise activation function. *Procedia Comput. Sci.* **2018**, *131*, 977−984.
(57) Wang, S.-H.; Muhammad, K.; Hong, J.; Sangaiah, A. K.; Zhang, Y.-D. Alcoholism identification via convolutional neural network based on parametric ReLU, dropout, and batch normalization. *Neural Comput. Appl.* **2020**, *32*, 665−680.
(58) Huber, P. J. Robust Estimation of a Location Parameter. *Ann. Math. Stat.* **1964**, *35*, 73−101.
(59) Kingma, D. P.; Ba, J. Adam: A Method for Stochastic Optimization. *arXiv* **2014**, DOI: 10.48550/arXiv.1412.6980.
(60) Abadi, M.; Agarwal, A.; Barham, P.; Brevdo, E.; Chen, Z.; Citro, C.; Corrado, G.S.; Davis, A.; Dean, J.; Devin, M.; Ghemawat, S.; Goodfellow, I.; Harp, A.; Irving, G.; Isard, M.; Jia, Y.; Jozefowicz, R.; Kaiser, L.; Kudlur, M.; Levenberg, J.; Mane, D.; Monga, R.; Moore, S.; Murray, D.; Olah, C.; Schuster, M.; Shlens, J.; Steiner, B.; Sutskever, I.; Talwar, K.; Tucker, P.; Vanhoucke, V.; Vasudevan, V.; Viegas, F.; Vinyals, O.; Warden, P.; Wattenberg, M.; Wicke, M.; Yu, Y.; Zheng, X. TensorFlow: Large-Scale Machine Learning on Heterogeneous Distributed Systems. *arXiv* **2016**, DOI: 10.48550/arXiv.1603.04467.
(61) Alqahtani, N.; Alzubaidi, F.; Armstrong, R. T.; Swietojanski, P.; Mostaghimi, P. Machine learning for predicting properties of porous media from 2d X-ray images. *J. Pet. Sci. Eng.* **2020**, *184*, No. 106514.
(62) Chen, T.; Guestrin, C. XGBoost: A Scalable Tree Boosting System. *Proceedings of the 22nd ACM SIGKDD International Conference on Knowledge Discovery and Data Mining*; 2016, pp 785−794..
(63) Cai, J.; Zhang, Z.; Wei, W.; Guo, D.; Li, S.; Zhao, P. The critical factors for permeability-formation factor relation in reservoir rocks: Pore-throat ratio, tortuosity and connectivity. *Energy.* **2019**, *188*, No. 116051.
(64) Goral, J.; Panja, P.; Deo, M.; Andrew, M.; Linden, S.; Schwarz, J.-O.; Wiegmann, A. Confinement Effect on Porosity and Permeability of Shales. *Sci. Rep.* **2020**, *10*, 49.
(65) Fu, J.; Wang, M.; Chen, B.; Wang, J.; Xiao, D.; Luo, M.; Evans, B. A data-driven framework for permeability prediction of natural porous rocks via microstructural characterization and pore-scale simulation. *Eng. Comput.* **2023**, *39*, 3895−3926.
(66) Hou, Z.; Cao, D.; Ji, S.; Cui, R.; Liu, Q. Enhancing digital rock image resolution with a GAN constrained by prior and perceptual information. *Comput. Geosci.* **2021**, *157*, No. 104939.
(67) Kamrava, S.; Tahmasebi, P.; Sahimi, M. Enhancing images of shale formations by a hybrid stochastic and deep learning algorithm. *Neural Networks.* **2019**, *118*, 310−320.

https://doi.org/10.1021/acsomega.3c10131
ACS Omega 2024, 9, 30205−30223